UNIVERSITÀ DEGLI STUDI DI PADOVA

Department of Information Engineering

Master's Degree in Automation Engineering

Robust Control of Parameter Fluctuations for Helical Motor

ヘリカルモータのパラメータ変動にロバストな制御法

Master's Candidate	Jessica Bergamo
Supervisor	Prof. Alessandro Beghi
Assistant Supervisor	Prof. Yasutaka Fujimoto

Padova, 11^{th} July 2017

Academic Year 2016/2017

To my dear family and friends.

千里の道も一歩から。
The road of a thousand ri starts from a step.
Japanese proverb.

Abstract

The scientific research introduces important advantages to society, with the improvement of every day life and the increase of industrial production: the idea of Industry 4.0 is becoming reality and the smart factories are growing all around the world. The changing of industrial manufacture, lead human work in close contact with robot. This collaboration yields benefit if it is ensure the safety of the operator. In this research, two important aspects of human and robot cooperation are analysed: the robustness of motion to parameter fluctuation and the control of motion suppression in the case of collision with an obstacle. A novel linear actuator, called Helical Motor, is proposed in order to achieve high performance and high back drivability with a small size. The design of control gains are performed in order to make system robust to model uncertainties. Furthermore, simulations and experiments are conducted, with the variation of model parameters, in order to verify the control performance. A new method for motion suppression, actuated when the impact with an obstacle occurs, is developed and it is based on the computation of kinetic energy. By simulation and experiment the robustness of the proposed approach to parameter fluctuations is evaluated.

Contents

List of Figures

List of Tables

Chapter 1

Introduction

1.1 Background

Nowadays, robots are largely used in many fields of human society, such as industries, medical treatment and human support [1]. Since human safety is one of the priority, actuators applied to these robot have to be powerful and safe at the same time.
Actually, electrical motors combining with high-reduction-ratio gears are largely used in industrial robots in order to achieve high torque easily. On the other hand, high-reduction-ratio gears produce large friction when the robot collides with an obstacle. Moreover, the high performances in a compact size actuator are very important to reach a good result.
A novel high thrust force actuator with high backdrivability that matches previous request is developed and it is called Helical Motor. Although this motor presents good tracking results, the analysis of parameter fluctuations are important to predict the motion, when a load is applied, and to prevent model instability. Therefore, the resulting trajectory can be correctly predicted and human can work in contact with robotic arm driven by helical motor in a safety way.

1.2 Research Objectives

The aim of this research is to analyse the situations in which human and robot cooperation could be dangerous. Precisely, the variation of motor parameters is performed in order to study the behaviour of helical motor in situations different from the nominal ones, while the suppression of joint motion, in case of collision with obstacle, is examined to prevent environmental damages or people's injuries. Regarding the latter, a new method is derived, based on kinetic energy computation; it can be applied in many situations because it does not require any adjustment of a threshold value to suppress the motion.
The organization of this thesis can be described as follows. Chapter 2 provides a brief introduction of helical motor, where the equations of motion, based on the linearised model, are displayed and the control laws are introduced.
In Chapter 3 the system robustness is analysed and the transfer functions of model are carried out. The model of system uncertain is introduced, precisely an inverse

multiplicative perturbation model is considered.
In Chapter 4 and Chapter 5 the kinematic and dynamic equations of one-link and two-link manipulators are implemented. In both cases, the Surface-mounted Permanent Magnet prototype is considered since it easily lends itself to be applied to a robotic arm.
Chapter 6 analyses the impact environment: the model of collision is described and the study of motion suppression is performed. In this context, a novel method to stop the motion, based on kinetic energy computation, is introduced and it is called Kinetic Energy Derivative Threshold .
In Chapter 7, the analysis of transfer functions is applied to the helical motor and the variation of mass, inertia and magnetic constant is observed at system output. It is extended in case of helical motor as joint of one-link and two-link manipulators. Moreover, under the variation of nominal mass, the results of motion suppression method are examined, considering both the proposed method (the Kinetic Energy Derivative Threshold) and an existing one (called Calculating Brake Time).
Chapter 8 describes the experiment related to parameter fluctuations considering the Interior Permanent Magnet prototype of helical motor and its response during motion suppression approaches.
Chapter 9 contains the conclusion of the research.

Chapter 2

The Helical Motor

In this chapter a brief description of helical motor is provided, the linearised model is introduced and the equations of the control system is described. In particular, the PD law is applied to force and position control and two Disturbance Observers are introduced to estimate disturbances in linear and rotary directions.

2.1 Introduction

The helical motor[2][3] is a novel high thrust force actuator with high backdrivability composed by a mover and a stator with spiral shape. Its main advantage is the capability of direct drive frictionless motion.
Permanent magnets are installed in the stator and two sets of three-phase windings are applied to the mover. Thrust force and torque are generated by controlling two inverters corresponding to the windings. The linear motion is extracted from screw motion in order to drive a load and the mover moves spirally in the stator.
Figure 2.1 illustrates the Interior Permanent Magnet (IPM) and Surface-mounted Permanent Magnet (SPM) prototypes of helical motor: the features of each type are described in Appendix C.
When the mover is in contact with the stator, by the attractive force, which acts between the stator core and the mover magnet, the system is in an uncontrolled state: in this case current is applied to the winding to float the mover from the stator. In this way, the magnetic levitation control is implement and the air gap between the stator and the mover is kept constant.
Using the electromagnetic force and the gap displacement between stator and mover, the levitation from the stator is performed and large frictional forces are avoid.
The spiral motor has two degree-of-freedom control. By controlling the air gap, the angular control provided by q-axis current will give forward or backward thrust.
Gap displacement x_g is computed through the difference between the linear position x and the angular position θ of the mover (as shown in Equation (2.1)) and it is measured by linear and rotary encoder:

$$x_g = x - h\theta \tag{2.1}$$

$$h = \frac{l_p}{2\pi} \tag{2.2}$$

where l_p is a lead length of the helix.
Total equations of the thrust f and torque τ are derived from the analysis of motion model, described in Appendix B. In order to achieve motion control, the approximate model linearised around $x_g = 0$ is considered.

$$f = K_{gn}x_g + K_{fn}I_d \quad (2.3)$$

$$\tau = K_{\tau n}I_q - hf \quad (2.4)$$

The d-axis current is represented by I_d and it mainly controls linear motion, whereas I_q describes q-axis current and it is related to rotary motion. The parameters K_{gn} , K_{fn} and $K_{\tau n}$ are the nominal values of magnetic force constant, thrust force constant and torque constant, respectively.
Considering the external thrust f_{dis} and torque τ_{dis} as disturbance affecting the mover, the helical motor equations of motion are described in (2.5) and (2.6) [1].

$$M\ddot{x} = f - f_{dis} \quad (2.5)$$

$$J\ddot{\theta} = \tau - \tau_{dis} \quad (2.6)$$

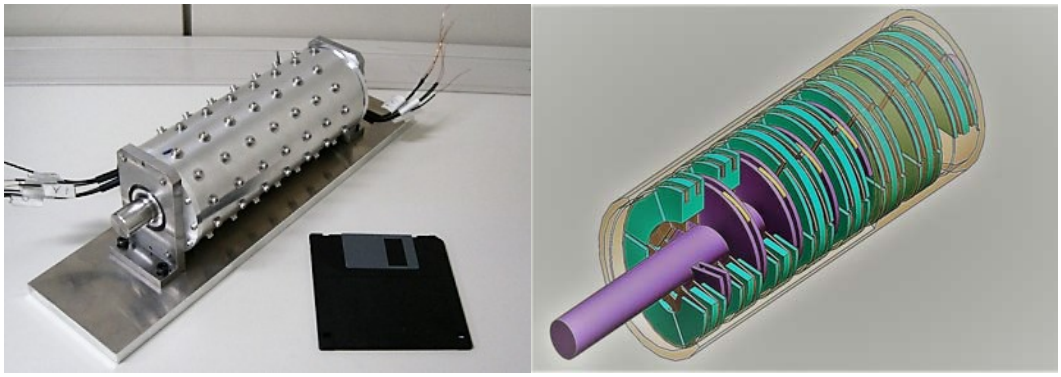

(a) IPM Spiral Motor (b) IPM Spiral Motor

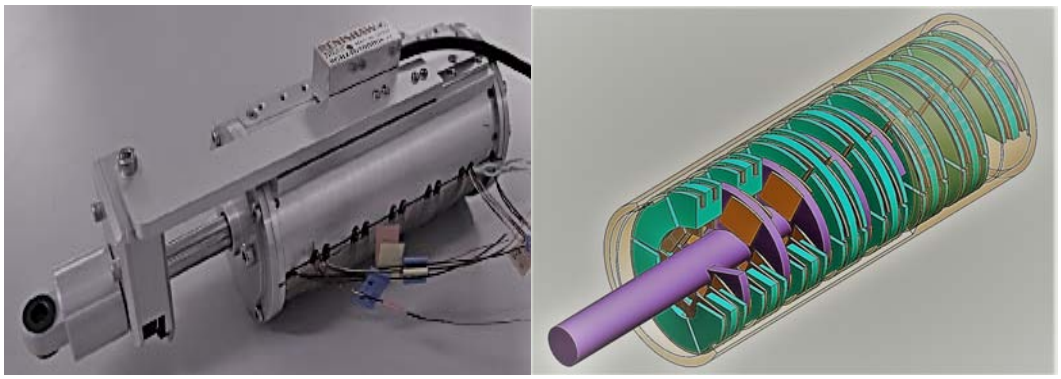

(c) SPM Spiral Motor (d) SPM Spiral Motor

Figure 2.1: IPM and SPM Helical Motor Prototype

[1] The total forces and torques acting to the system are the follows: $M\ddot{x}$ is the motor trust with mass M, $J\ddot{\theta}$ is the motor torque with inertia J, $K_f I_d$ is the force from d-axis current, $K_\tau I_q$ is the force from q-axis current and $K_g x_g$ represents the force generated during magnetic levitation.

2.2 Acceleration Control

To perform acceleration control, motion equations are used and dq-axis reference current equations are generated.
Solving Equations (2.5) and (2.6) and substituting I_d, I_q, $\ddot{x}$ and $\ddot{\theta}$ with the reference values I_d^{ref}, I_q^{ref}, $\ddot{x}^{ref}$ and $\ddot{\theta}^{ref}$, the acceleration control is achieved:

$$I_d^{ref} = \frac{1}{K_{fn}}\left(M_n\ddot{x}^{ref} - K_{gn}x_g + \hat{f}_{dis}\right) \tag{2.7}$$

$$I_q^{ref} = \frac{1}{K_{\tau n}}\left(J_n\ddot{\theta}^{ref} + h\left(K_{gn}x_g + K_{fn}I_d^{ref}\right) + \hat{\tau}_{dis}\right) \tag{2.8}$$

where M_n and J_n are mass and inertia nominal values, respectively.
The disturbance in the linear and rotary directions are estimated and compensated by two Disturbance Observer (DOB), described in Appendix A, whose equations are represented as follows.

$$\hat{f}_{dis} = \frac{w_d}{s+w_d}\left(K_{fn}I_d^{ref} + K_{gn}x_g + w_dM_n\dot{x}\right) - w_dM_n\dot{x} \tag{2.9}$$

$$\hat{\tau}_{dis} = \frac{w_{d\tau}}{s+w_{d\tau}}\left(K_{gn}x_g - h\left(K_{fn}I_d^{ref} + K_{gn}x_g\right) + w_{d\tau}J_n\dot{\theta}\right) - w_{d\tau}J_n\dot{\theta} \tag{2.10}$$

Here, s is the Laplace operator, w_d and $w_{d\tau}$ are the cut-off frequencies in linear and rotary motion. Figure 2.2 shown the two block diagrams of the disturbance observers.

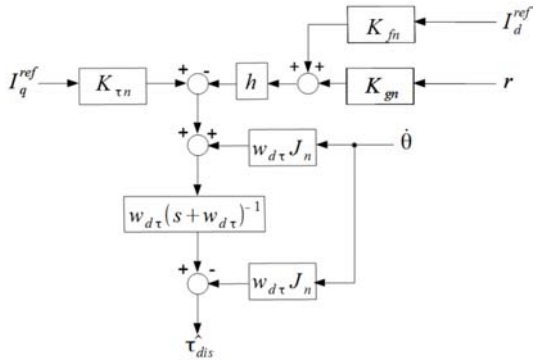

(a) Block Diagram of Rotation DOB

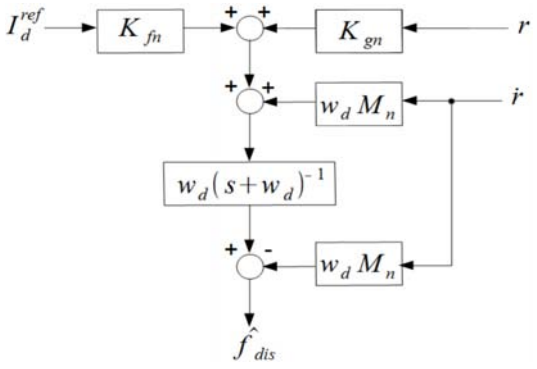

(b) Block Diagram of Linear DOB

Figure 2.2: Block Diagram of Linear and Rotation Disturbance Observers

2.3 Gap and Position Control

Perform magnetic levitation with a stable control of the gap displacement avoids any contact between the mover and the stator.
The gap controller consists of a PD-control that generates the gap displacement acceleration reference $\ddot{x}_g^{ref}$, as shown in Equation (2.11)

$$\ddot{x_g}^{ref} = K_{pg}\left(x_g^{ref} - xg\right) + K_{dg}\left(\dot{x}_g^{ref} - \dot{x}_g\right) \tag{2.11}$$

where K_{pg} and K_{dg} are designed by pole-placement of the gap response based on Equations (2.5), (2.6) and control law (2.11) [4]. The reference value x_g^{ref} is given by a zero power control[5].
Actually, a pair of complex conjugate poles are chosen in order to improve the robustness of control to parameter fluctuations.
Position controller is based on PD-control law

$$\ddot{x}^{ref} = K_{px}\left(x_{cmd} - x\right) + K_{dx}\left(\dot{x}_{cmd} - \dot{x}\right) + \ddot{x}_{cmd} \tag{2.12}$$

where $\ddot{x}^{ref}$ is the linear acceleration reference value and x_{cmd} is the position command of the mover. The PD-control gains, K_{px} and K_{dx}, are designed by pole placement of the ideal linear position response with the same procedure followed for the control gap gains. Also in this situation, a pair of complex conjugate poles are chosen.

2.4 Force and Torque Control

Regarding force control, a proportional law with damping effect is used.

$$\ddot{x}^{ref} = K_{pf}\left(f^{ref} - \hat{f}^{react}\right) - K_{df}\dot{x} \tag{2.13}$$

The proportional gain K_{pf} and the damping factor K_{df} are designed to improve the robustness. The symbol $\hat{f}^{react}$ represents the estimated reaction force computed by the Reaction Force Observer (RFOB) as follow.

$$\begin{aligned}\hat{f}^{react} &= \frac{w_{react}}{s + w_{react}}\left(K_{fn}I_d^{ref} + K_{gn}x_g + w_{react}M_n\dot{x}\right) \\ &\quad - w_{react}M_n\dot{x}\end{aligned} \tag{2.14}$$

The angular acceleration reference $\ddot{\theta}^{ref}$ is computed from the acceleration references $\ddot{x}^{ref}$ and $\ddot{x_g}^{ref}$.

$$\ddot{\theta}^{ref} = \frac{\ddot{x}^{ref} - \ddot{x}_g^{ref}}{h} \tag{2.15}$$

Chapter 3

Robustness of Control System

Robustness is an important problem in control-system design because real systems are affected by external disturbances, noises and parameter fluctuations[6]. In this chapter, the system transfer functions are analysed in order to understand which parameter mainly affect the motion. Moreover, the model applied to uncertainties is described.

3.1 Input Output Relationship

Actually, the real value of motor parameters is unknown and an approximation, given by the nominal value, is used.
For this reason, the analysis of modelling errors is necessary in order to improve the accuracy of results.
On the base of the block scheme in Figure 3.1, the transfer functions between the linear acceleration reference and the linear acceleration and the rotary acceleration are computed in (3.1) and (3.2), respectively.

$$\frac{\ddot{x}}{\ddot{x}^{ref}} = \frac{M_n s + M_n\, w_d}{M s + M_n\, w_d} \tag{3.1}$$

$$\frac{\ddot{\theta}}{\ddot{x}^{ref}} = \frac{N_{x\theta}}{D_{x\theta}} \tag{3.2}$$

$$\begin{aligned} N_{x\theta} = {} & J_n M s^4 + \left(\left(J_n M_n + J_n M\right) w_d + J_n K_{dg} M_n\right) s^3 \\ & + \left(J_n M_n w_d^2 + 2 J_n K_{dg} M_n w_d + J_n K_{pg} M_n\right) s^2 \\ & + \left(J_n K_{dg} M_n w_d^2 + 2 J_n K_{pg} M_n w_d\right) s + J_n K_{pg} M_n w_d^2 \end{aligned} \tag{3.3}$$

$$\begin{aligned} D_{x\theta} = {} & JMhs^4 + \left(\left(JM_n + J_n M\right) h w_d + J_n K_{dg} M h\right) s^3 \\ & + \left(J_n M_n h w_d^2 + \left(J_n M_n + J_n M\right) K_{dg} h w_d + J_n K_{pg} M h\right) s^2 \\ & + \left(J_n K_{dg} M_n h w_d^2 + \left(J_n M_n + J_n M\right) K_{pg} h w_d\right) s + J_n K_{pg} M_n h w_d^2 \end{aligned} \tag{3.4}$$

Here, the subscript n means the nominal value and the system quantities are introduced in Chapter 2. The relationships underline the importance of mass and inertia parameters to system outputs. Although Equation (3.1) shows the influence of mass, the variance of magnetic force constant and inertia are performed in order to test the response of the system to parameter uncertainties.
Finally the transfer function between the external force and the reference one is computed, as in Equation (3.5). The response is strictly connected with mass pa-

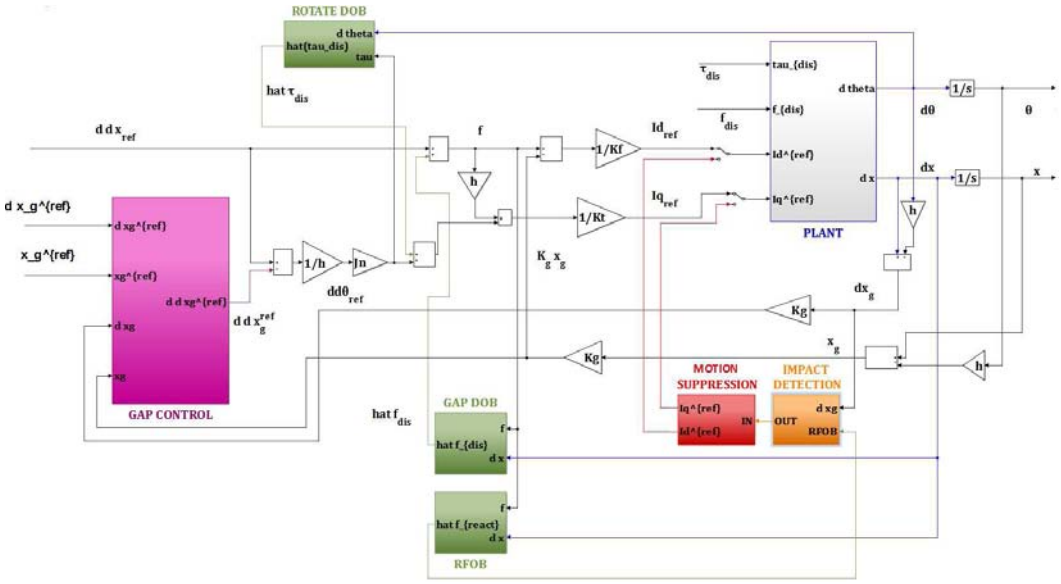

Figure 3.1: System Model

rameter.

$$\frac{f_{ex}}{f_{cmd}} = \frac{N_e(s)}{D_e(s)} \tag{3.5}$$

$$N_e(s) = K_{dmp}\,K_{pf}\,M_n\,s^2 + (K_{dmp}\,K_{pf}\,M_n\,w_d + K_{pf}\,K_{spr}\,M_n)\,s + K_{pf}\,K_{spr}\,M_n\,w_d \tag{3.6}$$

$$D_e(s) = Ms^3 + (((K_{pf}M+1)-K_{pf}M_n)\,M_n w_d + K_{df}M_n + K_{dmp})s^2 + ((K_{dmp}K_{pf}+K_{df})\;M_n w_d + K_{spr})s + K_{pf}K_{spr}M_n w_d \tag{3.7}$$

3.2 Modelling of System Uncertain

A mathematical model of any real system is an approximation of the true, physical reality of the system dynamics.
The uncertainty can be classified into two categories: disturbance signals (which includes input and output disturbance, sensor noise and actuator noise, etc.) and dynamic perturbations (that represents the discrepancy between the mathematical model and the actual dynamics of the system in operation).
The parameter fluctuations are modelled as an inverse input multiplicative perturbation, as described by (3.8), where P(s) denotes the actual, perturbed system and $P_n(s)$ a nominal model description of the physical system.

$$P_n(s) = P(1+\alpha) \tag{3.8}$$

The parameter α represents the uncertain that affects the real system. Figure 3.2 shows the block scheme of uncertainty model.

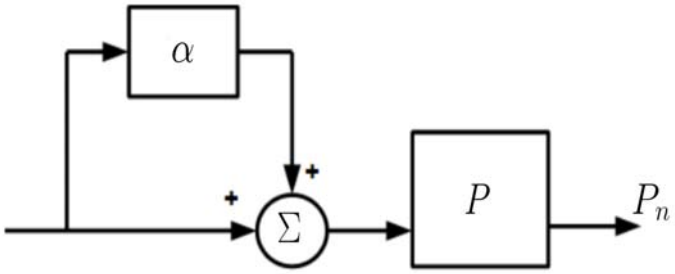

Figure 3.2: Model of Uncertainty

Chapter 4

One-link Manipulator

In this section a planar one-link manipulator is analysed by derivation of kinematics and dynamics equations[7][8]. The parameters used are described in Table 4.1, while Figure 4.1(a) shows the considered robotic arm with a SPM-type helical motors as manipulator joint.
In order to avoid misunderstandings in this chapter, the motor linear position and gap displacement are represented respectively by r and r_g, while x indicates the position in the 2-D space. Figure 4.2 displays an example of one-link manipulator actuating by the SPM prototype.

4.1 Mathematical Description

The considered set of generalized coordinates is $q = [q_1,\, q_2,\, q_3]^T = [r,\, \alpha,\, \beta]^T$ where α is the angle between link and helical motor, β is the angle between links and r represent the length of helical motor. The closed-chain system is virtually cut open at the connection point between the rotor final point and the links; then the kinetic energies are computed.

$$\begin{aligned} K_m &= \frac{1}{2}M_m\left(\dot{x}^2_{mover} + \dot{y}^2_{mover}\right) + \frac{1}{2}M_s\left(\dot{x}^2_{stator} + \dot{y}^2_{stator}\right) + \frac{1}{2}J_m\dot{\alpha}^2 + \frac{1}{2}J_s\dot{\alpha}^2 \\ &= \frac{1}{2}M_m\left(r^2\dot{\alpha}^2 + \dot{r}^2\right) + \frac{1}{2}\left(L_s^2\, M_s + J_m + J_s\right)\dot{\alpha}^2 \qquad (4.1) \\ K_a &= \frac{1}{2}M_a(\dot{x}^2_{link} + \dot{y}^2_{link}) + \frac{1}{2}J_a\dot{\beta}^2 \\ &= \frac{1}{2}\left(\frac{{L_3}^2}{2}\, M_a + J_a\right)\dot{\beta}^2 \qquad (4.2) \end{aligned}$$

where $(x_{stator},\, y_{stator})$ is the coordinate of stator final position, $(x_{mover},\, y_{mover})$ is the coordinate of mover final position and $(x_{link},\, y_{link})$ is the coordinate of link.

Their values are gauged as follow:

$$x_{stator} = L_s \cos(\alpha) \tag{4.3}$$
$$y_{stator} = L_s \sin(\alpha) \tag{4.4}$$
$$x_{mover} = r \cos(\alpha) \tag{4.5}$$
$$y_{mover} = r \sin(\alpha) \tag{4.6}$$
$$x_{link} = \frac{L_3}{2} \cos(\beta) + L_1 \tag{4.7}$$
$$y_{link} = \frac{L_3}{2} \sin(\beta). \tag{4.8}$$

The considered manipulator is a planar arm and the Lagrangian is obtained as sum of system kinetic energies:

$$L = K_m + K_a. \tag{4.9}$$

Equation of motion are computed using Lagrangian-Euler formulation, as in Equation (4.10) where F_i represents the generalized force.

$$\frac{d}{dt}\left(\frac{\partial L(q_i, \dot{q}_i)}{\partial \dot{q}_i}\right) - \frac{\partial L(q_i, \dot{q}_i)}{\partial q_i} = F_i. \tag{4.10}$$

The equation of the motion is derived from the analysis of the open-chain manipulator (Figure 4.1(b)) and it is expressed by Equation (4.11), with $B(q) \in \mathbb{R}^{3\times3}$ as the mass/inertia matrix and $C(q, \dot{q}) \in \mathbb{R}^{3\times1}$ as centrifugal/Coriolis matrix. The gravity term is ignored because a planar arm is considered.

$$B(q)\ddot{q} + C(q, \dot{q}) = F \tag{4.11}$$

The dynamical analysis require an additional term $J_c^T\lambda$ as vector of constraint forces, composed by the vector of Lagrange multiplier $\lambda \in \mathbb{R}^{2\times1}$ and the Jacobian of constraint equation $J_c \in \mathbb{R}^{2\times3}$.

$$B(q)\ddot{q} + C(q, \dot{q}) = F - J_c^T\lambda \tag{4.12}$$

where

$$B(q) = \begin{bmatrix} M_m & 0 & 0 \\ 0 & M_m r^2 + M_s L_s^2 + J_m + J_s & 0 \\ 0 & 0 & \frac{L_3^2 M_a}{4} + J_a \end{bmatrix} \tag{4.13}$$

$$C(q, \dot{q}) = \begin{bmatrix} -M_m r \dot{\alpha}^2 \\ 2M_m r \dot{r} \dot{\alpha} \\ 0 \end{bmatrix} \tag{4.14}$$

$$J_c = \begin{bmatrix} \cos(\alpha) & -r\sin(\alpha) & L_2\sin(\beta) \\ \sin(\alpha) & r\cos(\alpha) & -L_2\cos(\alpha) \end{bmatrix} \tag{4.15}$$

$$F = \begin{bmatrix} f_m & 0 & 0 \end{bmatrix}^T = \begin{bmatrix} (K_f I_d + K_g r_g) & 0 & 0 \end{bmatrix}^T \tag{4.16}$$

$$\lambda = \begin{bmatrix} \lambda_1 & \lambda_2 \end{bmatrix}^T. \tag{4.17}$$

Furthermore, the relation of acceleration at the constraint satisfies the following equation:

$$J_c\ddot{q} + \dot{J}_c\dot{q} = 0. \tag{4.18}$$

Finally contact force $F_{ex} \in \mathbb{R}^{2\times1}$ has to be considered when the end-effector of the robot reacts with the environment: in this situation the geometric Jacobian $J_{jacob} \in \mathbb{R}^{2\times3}$ is computed in order to translate the external force in joint space.

Then the motion equation is derived, as expressed by (4.19), where the dynamic of the helical motor is included:

$$B(q)\ddot{q} + C(q,\dot{q}) = F + J_c^T\lambda + J_{jacob}^T F_{ex} \tag{4.19}$$

$$\begin{bmatrix} B(\ddot{q}) & J_c^T & 0 \\ J_c & 0 & 0 \\ 0 & 0 & J_m \end{bmatrix} \begin{bmatrix} \ddot{q} \\ \lambda \\ \ddot{\theta} \end{bmatrix} = \begin{bmatrix} -C(\dot{q},q) + F + J_{jacob}^T F_{ex} \\ -\dot{J}_c\dot{q} \\ \tau_m \end{bmatrix}. \tag{4.20}$$

Here, τ_m is the total torque equation of helical motor expressed in Equation (2.4) and J_m is the moment of inertia about the motor rotation axis.

4.2 Workspace Position Control

The relationship between the motor liner position r and the angle β is expressed by cosine theorem.

$$r = \sqrt{L_2^2 + L_1^2 + 2L_1\,L_2\cos(\beta)} \tag{4.21}$$

By differentiating with respect to time, the relation (4.21) is expressed in the velocity dimension:

$$\dot{r} = -\frac{L_1\,L_2\,\sin(\beta)}{\sqrt{2L_1\,L_2\,\cos(\beta) + L_2^2 + L_1^2}}\dot{\beta}. \tag{4.22}$$

The control variable is represented by angle β and a Proportional-Derivative control law is implemented in order to compute the angular acceleration reference $\ddot{\beta}^{ref}$

$$\ddot{\beta}_{ref} = K_{p\beta}(\beta_{ref} - \beta) + K_{d\beta}(\dot{\beta}_{ref} - \ddot{\beta}) + \ddot{\beta}_{ref} \tag{4.23}$$

where

$$\beta = \operatorname{acos}\left(\frac{r^2 - {L_2}^2 - {L_1}^2}{2L_1\,L_2}\right) \tag{4.24}$$

$$\dot{\beta} = -\frac{r}{L_1\,L_2\sqrt{1 - \frac{\left(r1^2 - L_2^2 - L_1^2\right)^2}{4L_1^2\,L_2^2}}}\dot{r} \tag{4.25}$$

$$\beta_{ref} = \operatorname{acos}(\frac{r - L_1}{L_3}) \tag{4.26}$$

$$\dot{\beta}_{ref} = -\frac{L_3\dot{r}}{L_3\sqrt{(} - r^2 + 2L_1 r + L_3^2 - L_1^2)}. \tag{4.27}$$

Then, the relation concerning the reference acceleration $\ddot{r}^{ref}$ is obtained by differentiating with respect to time the Equation (4.22).

Parameter	*Character*	*Value*
Links Length	$L_1\, L_2\, L_3$	$0.19,\ 0.095\, 0.35\ [m]$
Links Length	$L_4\, L_5\, L_6$	$0.2, 0.08, 0.35\ [m]$
Nominal Mass of the Stator	M_s	$0.8\ [kg]$
Nominal Mass of the Mover	M_m	$0.5\ [kg]$
Nominal Mass of the Links	M_a	$0.42\ [kg]$
Nominal Inertia of the Stator	J_s	$1.12 \cdot 10^{-3}\ \left[kg \cdot m^2\right]$
Nominal Inertia of the Arm	J_a	$0.05\ \left[kg \cdot m^2\right]$
Nominal Inertia of the Mover	J_m	$2 \cdot 10^{-3}\ \left[kg \cdot m^2\right]$
Length of the Stator	L_s	$0.15\ [m]$
Length of the Helical Motor	r	$[0.1965\ ,\ 0.2565]\ [m]$

Table 4.1: Simulation Parameters of One-link and Two-link Manipulators

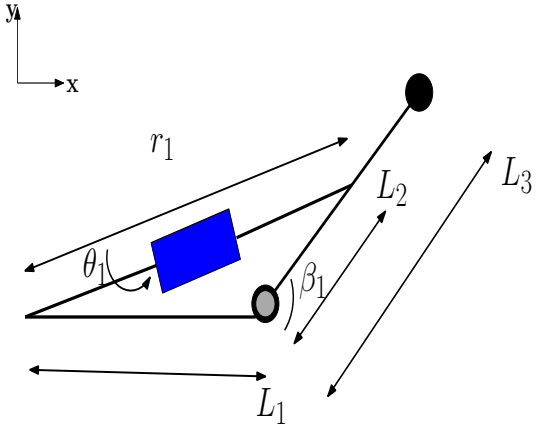

(a) One-link Manipulator, Close-Chain

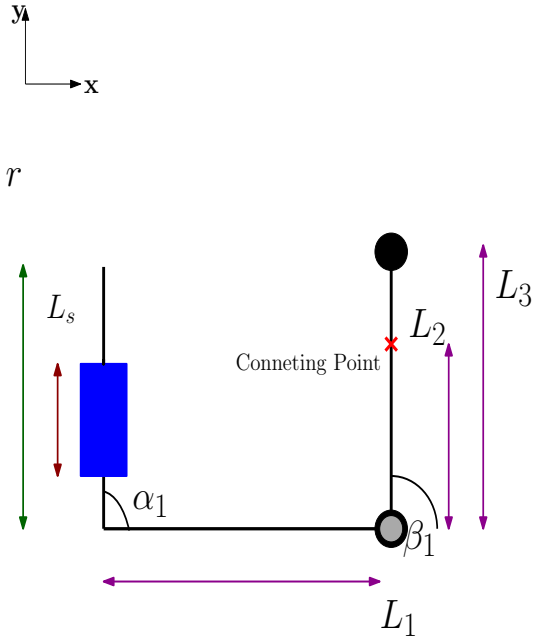

(b) One-link Manipulator, Open-Chain

Figure 4.1: One-link Manipulator

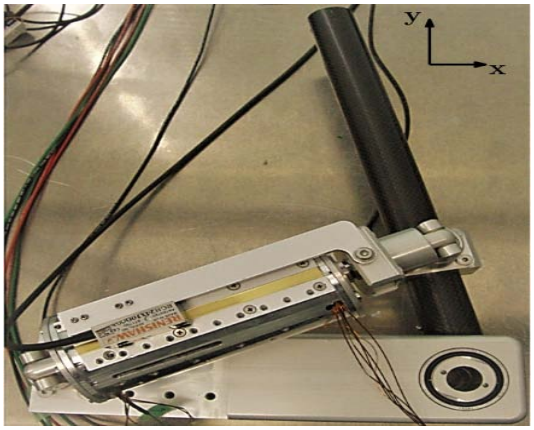

Figure 4.2: Example of 0ne-link Manipulator

Chapter 5

Two-link Manipulator

In this section the kinematic model and the derivation of dynamic for a planar two-link manipulator is carried out. Figure 5.1 shows the considered robotic arm, where two SPM-type helical motors are installed as manipulator joints[9][10]. The parameters used for derivation are summarized in Table 4.1. For simplicity, a planar manipulator is analysed and the gravitational elements can be neglected. In order to avoid misunderstandings, the motor linear position and gap displacement are represented by r and r_g respectively, while x indicates the position in the 2-D space.

5.1 Mathematical Description

Consider $q = \begin{bmatrix} q_1 & q_2 & q_3 & q_4 & q_5 & q_6 \end{bmatrix} = \begin{bmatrix} r_1 & r_2 & \alpha_1 & \alpha_2 & \beta_1 & \beta_2 \end{bmatrix}$ as the set of generalized coordinates, where α_i, $i = 1, 2$, is the angle between link and helical motor, β_i, $i = 1, 2$, is the angle between links and r_i, $i = 1, 2$, represent the length of helical motor. The closed-chain system is virtually cut open at the connection point between the rotor-end and links (as in Figure 5.1(b)) in order to get motion equations. Kinetic energies are computed as follows.

$$\begin{aligned} K_m &= \frac{1}{2} M_{m,1} (\dot{x}^2_{mover,1} + \dot{y}^2_{mover,1}) + \frac{1}{2} M_{s,1} (\dot{x}^2_{stator,1} + \dot{y}^2_{stator,1}) + \frac{1}{2} (J_{m1} + J_{s1}) \dot{\alpha}^2 \\ &+ \frac{1}{2} M_{m,2} (\dot{x}^2_{mover,2} + \dot{y}^2_{mover,2}) + \frac{1}{2} M_{s,2} (\dot{x}^2_{stator,2} + \dot{y}^2_{stator,2}) + \frac{1}{2} (J_{m2} + J_{s2}) \dot{\alpha}^2 \quad (5.1) \\ K_a &= \frac{1}{2} M_{a,1} (\dot{x}^2_{link,1} + \dot{y}^2_{link,1}) + \frac{1}{2} M_{a,2} (\dot{x}^2_{link,2} + \dot{y}^2_{link,2}) \quad (5.2) \end{aligned}$$

where the coordinates of stators, movers and links end point are (x_{stator},y_{stator}), (x_{mover},y_{mover}) and (x_{link},y_{link}), respectively.

$$x_{stator,1} = L_{s,1}\cos(\alpha_1) \tag{5.3}$$
$$y_{stator,1} = L_{s,1}\sin(\alpha_1) \tag{5.4}$$
$$x_{mover,1} = r_1\cos(\alpha_1) \tag{5.5}$$
$$y_{mover,1} = r_1\sin(\alpha_1) \tag{5.6}$$
$$x_{link,1} = L_1 + \frac{L_3}{2}\cos(\beta_1) \tag{5.7}$$
$$y_{link,1} = \frac{L_3}{2}\sin(\beta_1) \tag{5.8}$$
$$x_{stator,2} = L_1 + L_4\cos(\alpha_1) + L_{s,1}\cos(\alpha_1+\beta_2) \tag{5.9}$$
$$y_{stator,2} = L_4\sin(\alpha_1) + L_{s,1}\sin(\alpha_1+\beta_2) \tag{5.10}$$
$$x_{mover,2} = L_1 + L_4\cos(\alpha_1) + r_2\cos(\alpha_1+\beta_2) \tag{5.11}$$
$$y_{mover,2} = L_4\sin(\alpha_1) + r_2\sin(\alpha_1+\beta_2) \tag{5.12}$$
$$x_{link,2} = L_1 + \frac{L_3}{2}\cos(\beta_1) + \frac{L_6}{2}\cos(\beta_1+\beta_2) \tag{5.13}$$
$$y_{link,2} = \frac{L_3}{2}\sin(\beta_1) + \frac{L_6}{2}\sin(\beta_1+\beta_2). \tag{5.14}$$

The considered manipulator is a planar arm and the Lagrangian is obtained as sum of system kinetic energies:

$$L = K_m + K_a. \tag{5.15}$$

The equations of motion are computed using Lagrangian-Euler formulation, as in Equation (5.16) where F_i, with $i = 1...6$ represent the generalized force.

$$\frac{d}{dt}\left(\frac{\partial L(q_i,\dot{q}_i)}{\partial \dot{q}_i}\right) - \frac{\partial L(q_i,\dot{q}_i)}{\partial q_i} = F_i \tag{5.16}$$

They are extended to the open link chain as in (5.17), with $B(q) \in \mathbb{R}^{6\times6}$ as the mass/inertia matrix, $C(q,\dot{q}) \in \mathbb{R}^{6\times1}$ as centrifugal/Coriolis matrix and $J_c^T\lambda$ as vector of constraint forces, where $J_c \in \mathbb{R}^{4\times6}$ is the constraint Jacobian. The Lagrangian multiplier method is introduced to solve the equations of motion in the case of binding force, with $\lambda = [\lambda_1\,\lambda_2\,\lambda_3,\lambda_4]^T$ the vector of undetermined Lagrange multiplier.

$$B(q)\ddot{q} + C(q,\dot{q}) = F + J_c^T\lambda \tag{5.17}$$
$$F = \begin{bmatrix} f_{m1} & f_{m2} & 0 & 0 & 0 & 0 \end{bmatrix}^T$$
$$= \begin{bmatrix} (K_{f1}I_{d1} + K_{g1}r_{g1}) & (K_{f2}I_{d2} + K_{g2}r_{g2}) & 0 & 0 & 0 & 0 \end{bmatrix}^T \tag{5.18}$$

Furthermore, the relation of acceleration at the constraint satisfies the following equation:

$$J_c\ddot{q} + \dot{J}_c\dot{q} = 0. \tag{5.19}$$

Finally, contact force $F_{ex} \in \mathbb{R}^{2\times1}$ has to be considered when the robot end-effector reacts with the environment: in this situation the geometric Jacobian $J_{jacob} \in \mathbb{R}^{2\times6}$ is considered in order to translate the external force in joint space.
Then, the motion equation is derived, as shown by (5.20), where the dynamic of

the helical motor is considered:

$$D(q)\ddot{q} + C(q,\dot{q}) = F + J_c^T\lambda + J_{jacob}^T F_{ex} \tag{5.20}$$

$$\begin{bmatrix} D(\ddot{q}) & J_c^T & 0 \\ J_c & 0 & 0 \\ 0 & 0 & J_m \end{bmatrix} \begin{bmatrix} \ddot{q} \\ \lambda \\ \ddot{\theta} \end{bmatrix} = \begin{bmatrix} -C(\dot{q},q) + F + J_{jacob}^T F_{ex} \\ -\dot{J}_c\dot{q} \\ \tau_m \end{bmatrix} \tag{5.21}$$

in which τ_m is the total torque equation of helical motor expressed in (2.4) and $J_m = diag\,(J_{m,1}\, J_{m,2})$ is the moment of inertia about the motor rotation axis of joint 1 and joint 2.

5.2 Workspace Position Control

The geometric Jacobian, that express the relation between end-effector and joint velocity, is computed applying the derivation by time of the kinematic equation (5.22):

$$x_e = \begin{bmatrix} L_1 + L_3\,\cos(\beta_1) + L_6\,\cos(\beta_1+\beta_2) \\ L_3\,\sin(\beta_1) + L_6\,\sin(\beta_1+\beta_2) \end{bmatrix} \tag{5.22}$$

where the relationship between the angle β_i, $i = 1,2$, and the motor length r_i, $i = 1,2$, is obtained by the cosine formula

$$\beta_1 = \arccos\left(\frac{r_1^2 - L_1^2 - L_2^2}{2L_1L_2}\right) \tag{5.23}$$

$$\beta_2 = \arccos\left(\frac{r_2^2 - (L_3-L_4)^2 - L_5^2}{2(L_3-L_4)L_5}\right). \tag{5.24}$$

Then, the differential kinematic equation is

$$\dot{x}_e = J_{jacob}(q)\dot{r}. \tag{5.25}$$

Finally, by deriving the Equation (5.25) with respect to time, the relation describing joints linear acceleration, as a function of end-effector velocity and acceleration, is obtained

$$\ddot{r} = J_{jacob}(q)^{-1}\ddot{x}_e - J_{jacob}(q)^{-1}\dot{J}_{jacob}(q)\dot{x}_e. \tag{5.26}$$

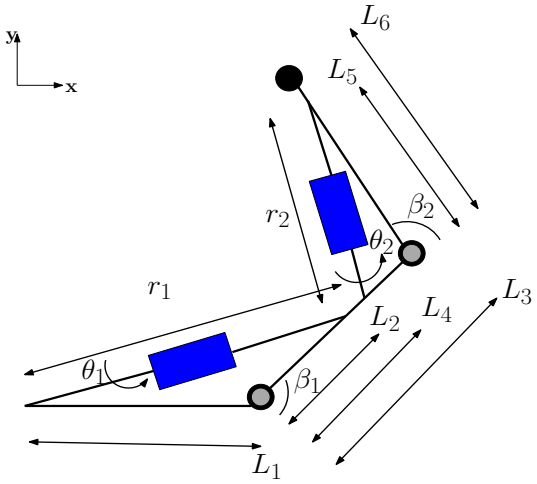

(a) Two-link Manipulator Close-Chain

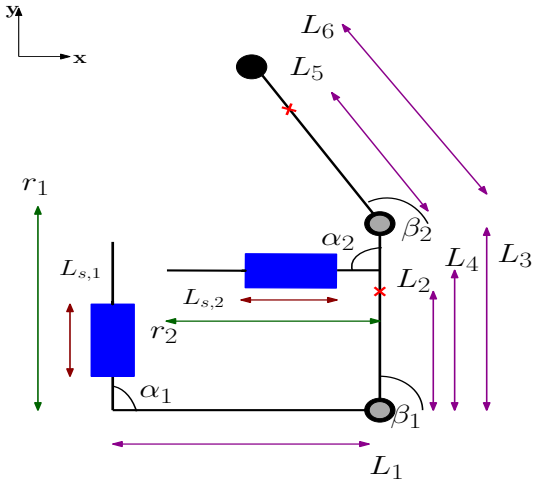

(b) Two-link Manipulator Open-Chain

Figure 5.1: Two-link Manipulator

Chapter 6

Impact Control

In this section, the reaction force generated by the contact between an obstacle and the robot end-effector is considered. A mathematical model of impact is provided and the performance of two approaches for the suppression are analysed. Precisely, the Kinetic Energy Derivative Threshold method is proposed in order to stop the motion in all condition, with an universal threshold value; while the Calculating Brake Time is an existing method based on momentum computation, whose main purpose is to reduce the strength of the force. Finally, an impact detection method, based on gap power, is described.

6.1 Model of Impact

The impact force is generated by the contact between the robot and obstacle and it is strictly related to the kinetic energy of the manipulator. The environment interacting with the end-effector can be represented by spring-damper model:

$$f^{react} = K_s x + K_d \dot{x} \tag{6.1}$$

where the spring coefficient, K_s, and the viscous friction coefficient, K_d, are related to the considered environment. Figure 6.1 illustrates the impact model.
In general $K_s > K_d$ and high value of spring gain leads to large value of reaction force. Moreover, the impact force is related to system kinetic energy: when the collision takes place, the robot kinetic energy is mainly transformed in thermal energy, that can cause damages and deformations. For this reason fast motion suppression method is required.

6.2 Motion Suppression

Suppressing the impact force and motion is necessary to preserve the surrounding environment and ensure human safety. In the past decades, many researchers studied the avoidance of collision forces. A mechanism was proposed to suppress them in [11], where the impact force is passively reduced without any control. Sami Haddadin et al. [12] analysed many reaction strategies to decrease the potential danger. Concerning the simple force control method, it could not be sufficient to guarantee the work safety.
In this cases, the consumption of all kinetic energy is important in order to suppress

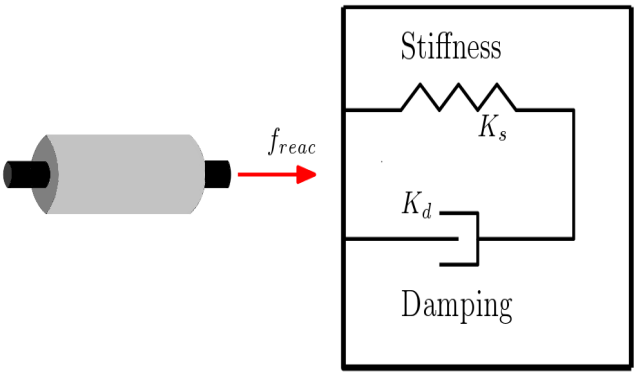

Figure 6.1: Impact Model

the motion and the proposed method has to be applied universally, since different situations could occur.
Using helical motor, a suited procedure to consume kinetic energy is obtained by applying the maximum brake current in the opposite direction of motion after the collision detection and shifting to the force control. In helical motor, it is necessary to change in force control when the brake control is applied because it could lead to gap instability due to high current values.

6.2.1 Kinetic Energy Derivative Threshold

The Kinetic Energy Derivative Threshold (KEDT) is an automatic threshold method to suppress motion[13].
The kinetic energy, expressed by (6.2) can be calculated in real time by measuring the spiral motor speed. The aim of this control is to suppress impact and to consume all system kinetic energy.
An automatic threshold is used, based on the derivative of kinetic energy which is computed as in equation (6.3).

$$E = \frac{1}{2} M \cdot \dot{x}^2 \tag{6.2}$$

$$\dot{E} = M \cdot \dot{x} \cdot \ddot{x} \tag{6.3}$$

In order to generate maximum thrust, a limit value for the d-axis current is provide in opposite direction of the motor during brake control. At the same time, the q-axis current achieves limit value for stabilizing gap because the generated high thrust makes lose the compensation given by disturbance observer. A maximum torque is supplied in the direction of stabilization, that is, the one for which x_g converges to 0.
Finally, the motion is suppressed switching to the force control after the brake control by governing the current with the acceleration control system described in Section 2.2.
At impact time, if the kinetic energy increases and its derivative is positive, the motion is stopped by brake control. The system equation that describes the current

behaviour to suppress motion is shown in (6.4) and (6.5).

$$I_d^{ref} = \begin{cases} -I_d^{max}\text{sign}(\dot{x}) & \dot{E} > 0 \\ \frac{1}{K_{fn}}\left(M_n\ddot{x}^{ref} - K_{gn}x_g + \hat{f}_{dis}\right) & \dot{E} < 0 \end{cases} \tag{6.4}$$

$$I_q^{ref} = \begin{cases} I_q^{max}\text{sign}(\dot{x}_g) & \dot{E} > 0 \\ \frac{1}{K_{\tau n}}\left(J_n\ddot{\theta}^{ref} + h\left(K_{gn}x_g + K_{fn}I_d^{ref}\right) + \hat{\tau}_{dis}\right) & \dot{E} < 0 \end{cases} \tag{6.5}$$

6.2.2 Calculating Brake Time

The Caluculating Brake Time (CBT) method[14] is based on momentum computation because, when kinetic energy is calculated in real time, the influence of pseudo-derivative could be not negligible. The momentum is derived by integrating both sides of the motion equation:

$$M\dot{x} = \int \left(K_f I_d + K_g x_g - f_{ex}\right) dt. \tag{6.6}$$

If it can be assumed that the external force and the magnetic attractive force do not change while the braking force is applied, then impulse is the product of the brake time,

$$M\dot{x}_{imp} = \left(K_f I_d^{limit} + K_g x_{g_{imp}} - f_{ex_{imp}}\right)\Delta t \tag{6.7}$$

where x_{imp}, $x_{g_{imp}}$, and $f_{ex_{imp}}$ represent the collision velocity, the collision gap displacement and the impact force, respectively.
Finally, the braking time to consume kinetic energy is expressed by the following equation

$$\Delta t = \left| \frac{M\dot{x}_{imp}}{K_f I_d^{limit} + K_g x_{g_{imp}} - f_{ex_{imp}}} \right|. \tag{6.8}$$

6.3 Impact Detection using Gap Power

The gap energy is a specific element of helical motor and it can be used in order to detect the time of impact. The power is obtained by derivative of the estimated work, $\mathtt{L}$, that can be exerted on the gap by external force, as described in the following equations

$$\mathtt{L} = \int \hat{f}_{ex} dx_g \tag{6.9}$$

$$\Delta\mathtt{L} = \frac{d\mathtt{L}}{dt} = \hat{f}_{ex}\dot{x}_g \tag{6.10}$$

where $\hat{f}_{ex}$ is the estimated force and $\dot{x}_g$ is the gap velocity.
The gap velocity is set instead of the mover velocity $\dot{x}$ because, even when x moves greatly, the change in x_g is small due to the gap control, so $\Delta\mathtt{L}$ can be maintained near 0. The proposed signal $\dot{x}_g$ changes greatly only when a sharp disturbance, such as a collision, is added.
Hence, the gap power becomes a good indicator since it reacts only at the collision time.

Chapter 7

Simulation

The system robustness to parameter fluctuation is tested in simulation for the single helical motor and for the one-link and two-link robotic arms.
Two different situations are analysed: the contactless case and the contact one.
In the first it is assumed no contact between the end-effector and obstacle, then position and gap control affected by parameter fluctuations are checked. The second considers the contact with an obstacle and the performance of the proposed motion suppression method are analysed.

7.1 Introduction

In this section, the estimated behaviour under parameter fluctuations of helical motor, one-link and two-link manipulators are analysed.
In all situations, the simulator code is implemented in C language and the plant variables are calculated using Runge-Kutta method, after the realization of motion equations.
Regarding the contact case, an hard obstacle is placed in front of the motor and the collision is realized by a spring damper model, with $K_{spr} = 100,000\,[N/m]$ and $K_{dmp} = 10\,[N \cdot s/m]$ as spring and damper coefficient, respectively. Furthermore, the achievements of the proposed procedure is compared with a method for impact force suppression, called Calculating Brake Time (CBT). In Calculating Brake Time the momentum of the collision is recorded where it is assumed that all variables, except speed, are invariant.

7.2 Helical motor

In this section, IPM and SPM prototypes are considered, whose model parameters are shown in Table 7.1 and Table 7.2, respectively.
The same control system is implemented for both motors in order to test the adaptability of controllers when the model parameters change. The control gains are designed by pole-placement of position and gap responses based on motion equations (2.5), (2.6) and control laws (2.12), (2.11) of position and gap. The gain values are shown in Table 7.3.
Furthermore, a trapezoidal move profile is used for the creation of velocity reference and noisy input variables are realized for a more realistic simulation.
Before starting trajectory tracking, the magnetic levitation has to be performed in order to stabilize gap displacement. In simulation it is assumed that the gap stabilization is done, in agreement with experiment results, and a null gap initial displacement is set.
Regarding the contact case, the obstacle is placed at 0.009 [m] from the motor end-effector in order to emulate the experiment setting.

Parameter	*Character*	*Value*
Nominal Thrust Constant	K_{fn}	11.15 $[N/A]$
Nominal Torque Constant	$K_{\tau n}$	0.105 $[Nm/A]$
Nominal Magnetic Constant	K_{gn}	122000 $[N/m]$
Nominal Length of the Screw	l_p	$22 \cdot 10^{-3}$ $[m]$
Nominal Mass of the Mover	M_n	0.7 $[kg]$
Nominal Inertia of the Mover	J_n	$13 \cdot 10^{-5}$ $\left[kg \cdot m^2\right]$
Cut-off Frequency of Thrust Disturbance Observer	w_d	500 $[rad/s]$
Cut-off Frequency of Torque Disturbance Observer	$w_{d\tau}$	500 $[rad/s]$
Cut-off Frequency of Reaction Force Observer	w_{react}	300 $[rad/s]$
Cut-off Frequency of Low Pass Filter Pseudo Derivative	w_{diff}	2000 $[rad/s]$
Cut-off Frequency of Kinetic Energy Pseudo Derivative	w_E	40 $[rad/s]$
Sampling Period of Simulation	T_s	1.0 $[\mu s]$
Sampling Period of Controller	T_c	66.6 $[\mu s]$
Limit d-axis Current	I_d^{lim}	40 $[A]$
Limit q-axis Current	I_q^{lim}	40 $[A]$
Gap Power Threshold	$\Delta \mathrm{L}_{thr}$	0.002 $[W]$

Table 7.1: Simulation Parameters of IPM Prototype

Parameter	*Character*	*Value*
Nominal Thrust Constant	K_{fn}	9.42 $[N/A]$
Nominal Torque Constant	$K_{\tau n}$	0.194 $[Nm/A]$
Nominal Magnetic Constant	K_{gn}	566000 $[N/m]$
Nominal Length of the Screw	l_p	$20 \cdot 10^{-3}$ $[m]$
Nominal Mass of the Mover	M_n	0.3 $[kg]$
Nominal Inertia of the Mover	J_n	$2 \cdot 10^{-3}$ $\left[kg \cdot m^2\right]$
Cut-off Frequency of Thrust Disturbance Observer	w_d	600 $[rad/s]$
Cut-off Frequency of Torque Disturbance Observer	$w_{d\tau}$	600 $[rad/s]$
Cut-off Frequency of Reaction Force Observer	w_{react}	300 $[rad/s]$
Cut-off Frequency of Low Pass Filter Pseudo Derivative	w_{diff}	2000 $[rad/s]$
Sampling Period of Simulation	T_s	10 $[\mu s]$
Sampling Period of Controller	T_c	66.0 $[\mu s]$
Limit d-axis Current	I_d^{ref}	40 $[A]$
Limit q-axis Current	I_q^{ref}	40 $[A]$

Table 7.2: Simulation Parameters of SPM Prototype

Parameter	*Character*	*Value*
Proportional Gain of Gap Controller	K_{pg}	42925.0
Derivative Gain of Gap Controller	K_{dg}	410.0
Proportional Gain of Position Controller	K_{px}	1217.0
Derivative Gain of Position Controller	K_{dx}	67.0
Proportional Gain of Force Controller	K_{pf}	0.1
Damping gain of Force Controller	K_{df}	200.0

Table 7.3: Simulation Parameters of Control

7.2.1 Contactless Case

The transfer functions between acceleration and acceleration reference, computed in Section 3.1, underline the important role of mass and inertia parameters, then M_n and J_n variation are tested. Moreover, the magnetic constant K_g is considered because it is closely linked to gap displacement.
Concerning the IPM prototype, a variation $\alpha = |0.7|$ of nominal value in Equation (3.8) is applied and the results are displayed in Figures 7.1 .
Concerning nominal mass, low values lead gap error to high displacement, especially when the linear position is not constant; also the position tracking is affected by mass and the error is small when velocity is not constant. The nominal inertia affects the gap tracking as mass but it induces high current in q-axis values, since both variables are connected to rotary motion. The cause of this behaviour could

be found in the introduced quantized noise in the control variables.
The results shows that the system is more robust to magnetic constant fluctuation because it is not directly related to system output variables, as mass and inertia are. Figure 7.2 shows the simulation results of SPM helical motor, where $\alpha = |0.5|$ is considered. The same achievements of IPM prototype are reached: the position tracking is more sensitive to mass variation and gap displacement has large oscillations for M_n and J_n small. Also in this situation, a higher inertia produces important oscillations in q-axis current.

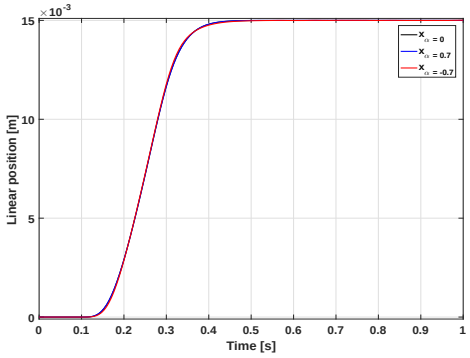

(a) Linear Position, Mass Variation

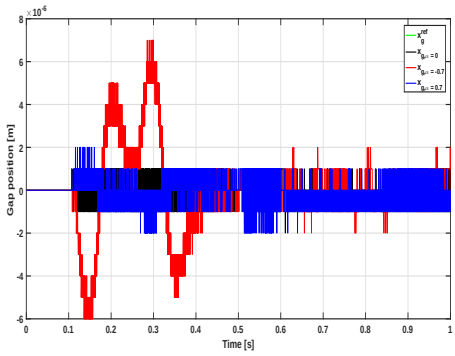

(b) Gap Displacement, Mass Variation

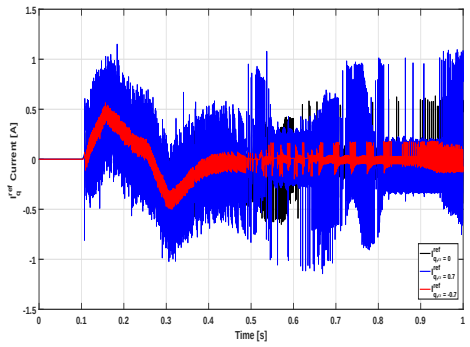

(c) I_q^{ref} Current, Inertia Variation

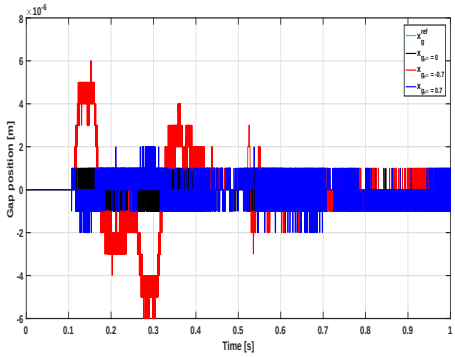

(d) Gap Displacement, Inertia Variation

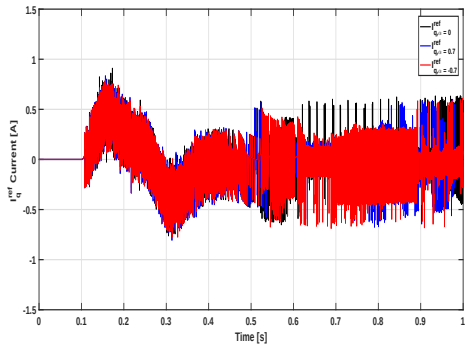

(e) I_q^{ref} Current, Magnetic Constant Variation

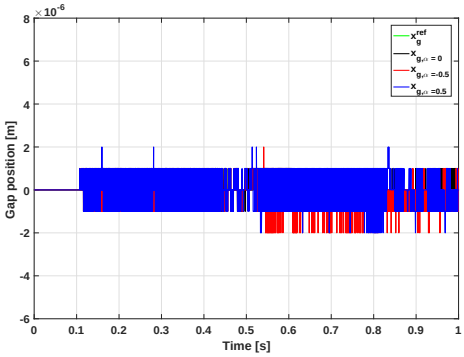

(f) Gap Displacement, Magnetic Constant Variation

Figure 7.1: IPM Helical Motor, Parameter Variations

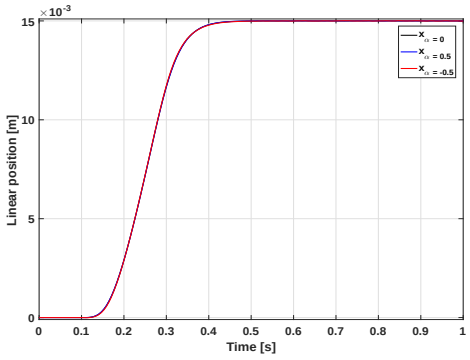

(a) Linear Position, Mass Variation

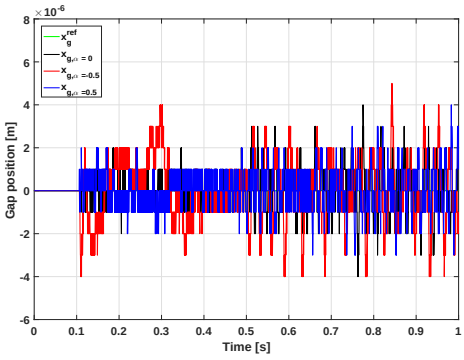

(b) Gap Displacement, Mass Variation

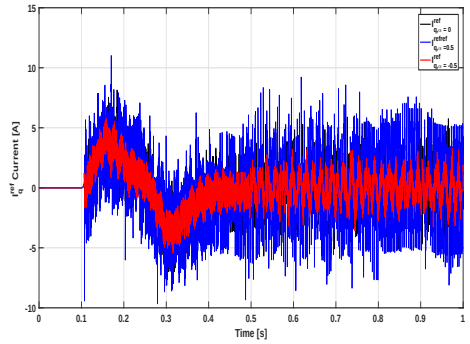

(c) I_q^{ref} Current, Inertia Variation

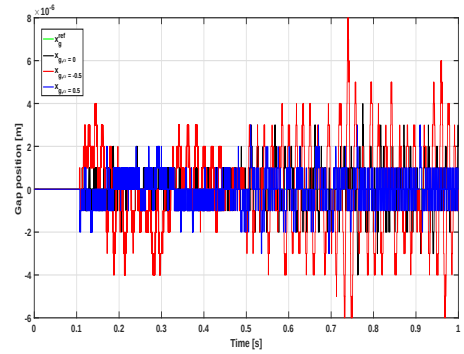

(d) Gap Displacement, Inertia Variation

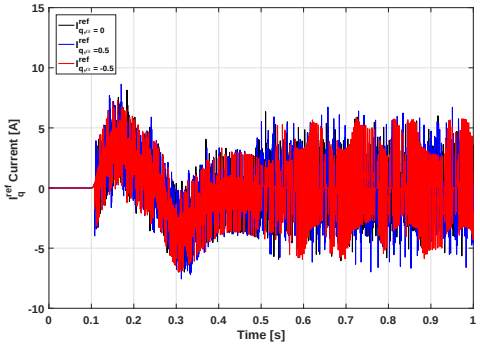

(e) I_q^{ref} Current, Magnetic Constant Variation

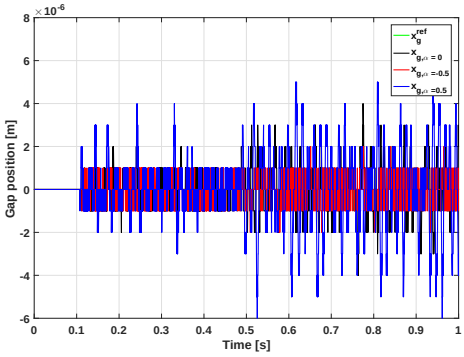

(f) Gap Displacement, Magnetic Constant Variation

Figure 7.2: SPM Helical Motor, Parameter Variations

7.2.2 Contact Case

The transfer function (3.5) shows that the mass parameter plays an important role in force response and the proposed method, based on kinetic energy computation, closely depends on mass. For those reasons, only the mass variation is performed in order to test the results of motion suppression.
In Figure 7.3 the estimated responses of kinetic energy, linear velocity and reaction force of IPM helical motor are displayed with the uncertainty value of $|0.5|$.

According to the experimental case, the value of force reference is zero and the Gap Power method, with threshold of $0.002\,[W]$, is used for the detection.
The KEDT method has smaller undershoot than the CBT one in linear velocity, when the collision takes place. Furthermore, the kinetic energy converges faster to zero.
The reaction force is higher in KEDT, since its aim is to suppress motion, and not to reduce the collision force. Considering $\alpha = -0.5$, the responses given by the two methods are the same, the reason can be guessed in the small value of mass.
The proposed method is more robust to nominal mass variation and regarding parameters related to the motion, high values lead to better performance.

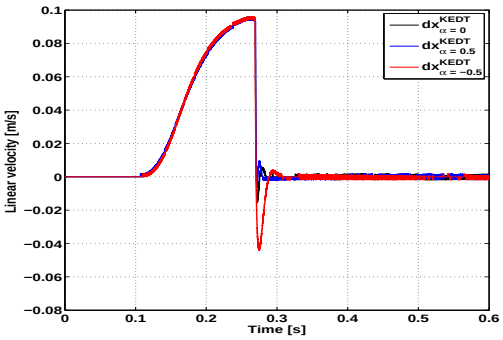

(a) Kinetic Energy Derivative Threshold, Velocity

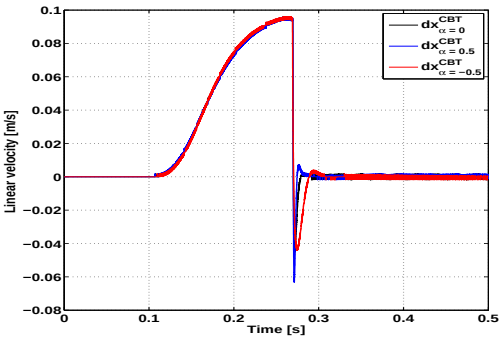

(b) Calculating Brake Time, Velocity

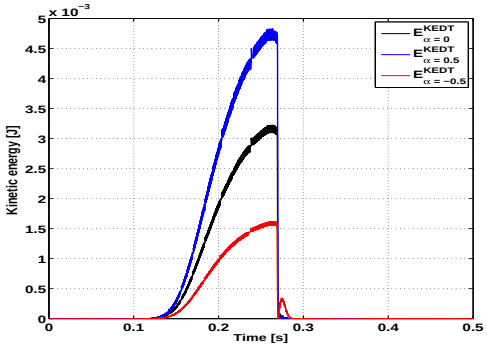

(c) Kinetic Energy Derivative Threshold, Kinetic Energy

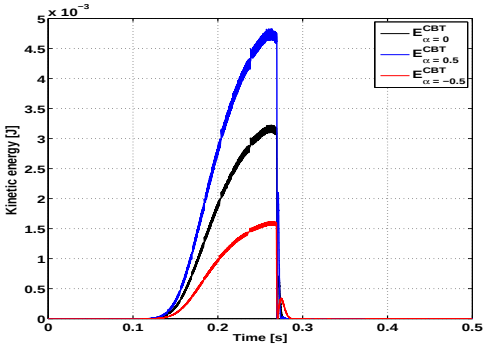

(d) Calculating Brake Time, Kinetic Energy

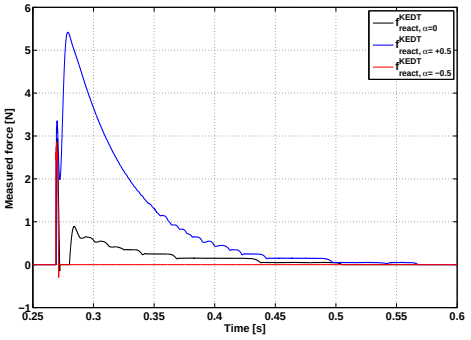

(e) Kinetic Energy Derivative Threshold, Reaction Force

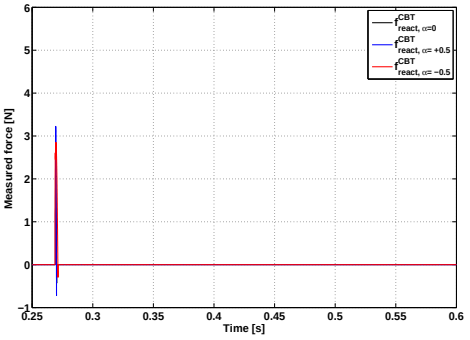

(f) Calculating Brake Time, Reaction Force

Figure 7.3: IPM Prototype, Contact Case

7.3 One-Link Manipulator

In this section the one-link manipulator moved by helical motor is analysed. In particular, only the SPM prototype is considered since it is more suitable as robot actuator than IPM type. The plant and control values are shown in Table 7.4. Input signals are not affected by noise for a better analysis and a trapezoidal move profile is computed. Regarding the obstacle position, it is set far from motor initial point, as illustrated by Figure 7.4.

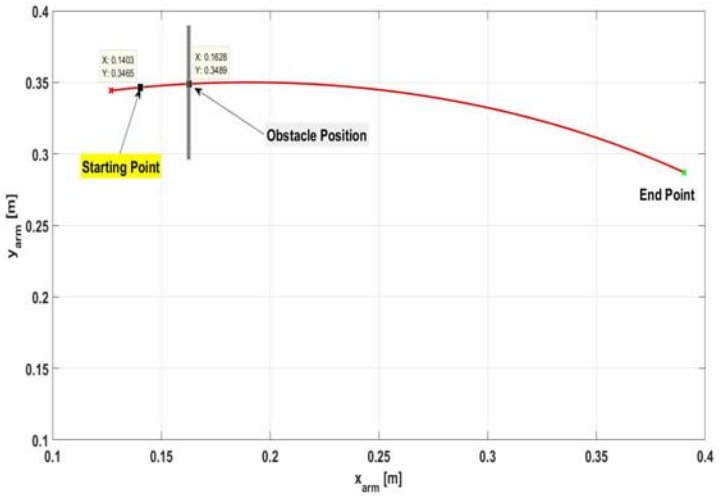

Figure 7.4: One-link Manipulator, Obstacle Position

7.3.1 Contactless Case

As suggested by Section 3, the nominal mass variation follows Equation (3.8) and the value α equal to 0, 3 and 7 is applied.
When the nominal and real values coincide, the system is unstable. The reason can be guessed in the mass matrix: in this case its value is smaller and the disturbance observer can not compensate the error[15]. In Figure 7.5 is described the system behaviour with uncertainty mass. The value $M_n = 4\,[Kg]$ ($\alpha = 7$) is chosen for the next simulations in order to analysed the variation without any error given by mass parameter.
Concerning nominal inertia, a variation of $\alpha = |0.7|$ is imposed and system response is displayed in Figure 7.6. The trajectory tracking is not affected both in joint and end-effector domains. The gap displacement is different from its reference value when the arm velocity is not constant. Under the same condition the q-axis current has higher values if the nominal inertia is large: since both inertia and I_q^{ref} are related to rotary motion, wider current has to be provided when velocity change.
Finally, the magnetic constant parameter is varied with $\alpha = |0.7|$ as in Figure 7.7. In this situation there are not any changes in trajectory and velocity tracking with respect to the reference value. Moreover, the q-axis current does not present large value when velocity is not constant: K_g is strictly related to r and θ displacement.

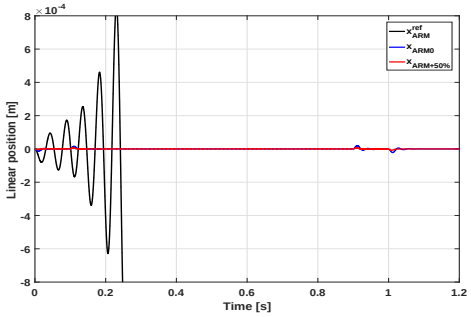

(a) Arm Trajectory Tracking Error in x-direction

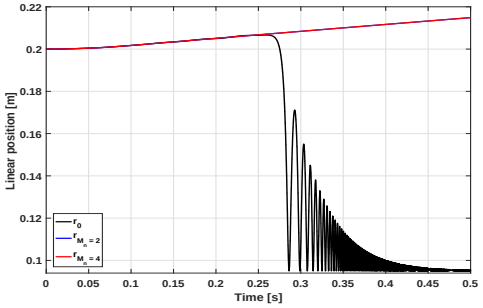

(b) Motor Trajectory Tracking

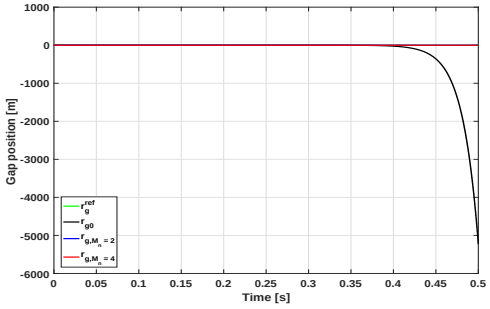

(c) Gap Displacement

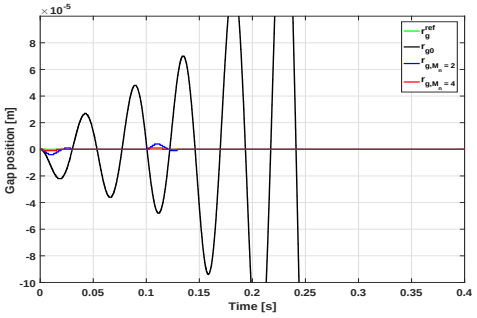

(d) Detail of Gap Displacement

Figure 7.5: One-link Manipulator, Nominal Mass Variation

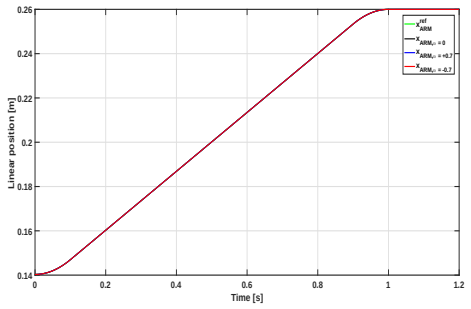

(a) Arm Trajectory Tracking in x-direction

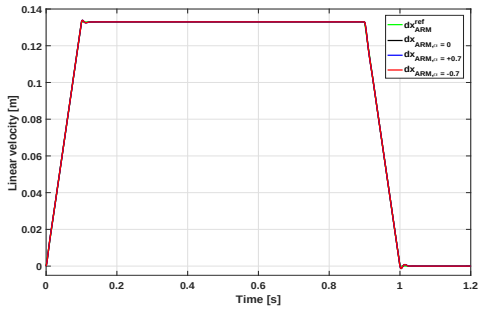

(b) Arm Velocity Tracking in x-direction

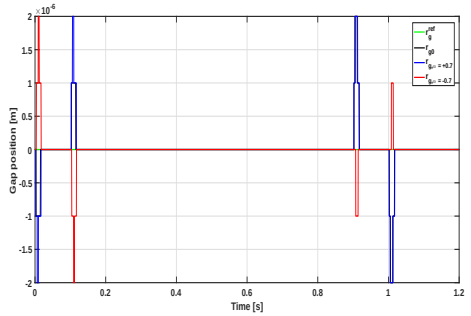

(c) Gap Displacement

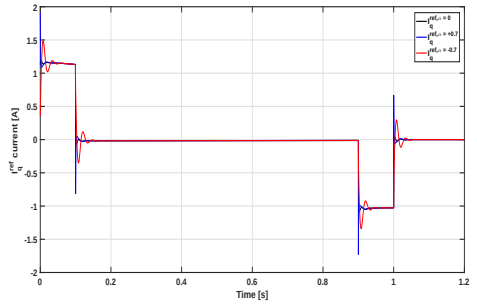

(d) I_q^{ref} Current

Figure 7.6: One-link Manipulator, Nominal Inertia Variation

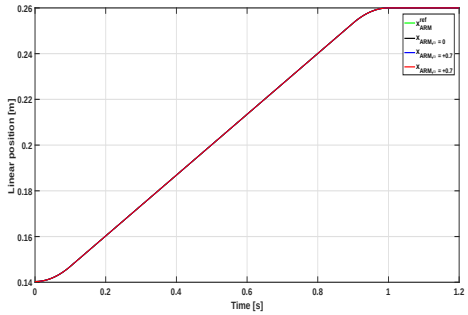

(a) Arm Trajectory Tracking in x-direction

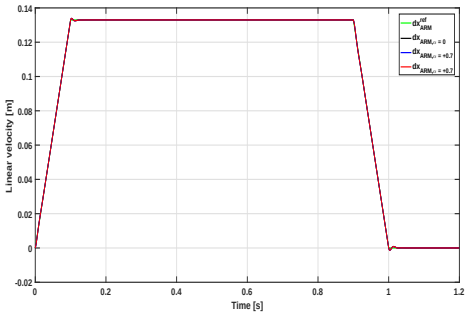

(b) Arm Velocity Tracking in x-direction

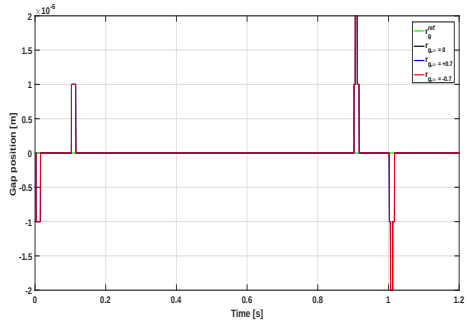

(c) Gap Displacement

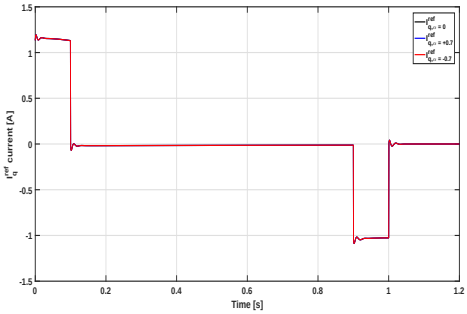

(d) I_q^{ref} Current

Figure 7.7: One-link Manipulator, Nominal Magnetic Constant Variation

7.3.2 Contact Case

The nominal mass is varied considering the uncertainty parameter α equal to 3, 7 and 11. In this situation the impact detection is based on the force value and not on the gap power threshold because, since it is an ideal case, the errors given by detection are avoided. The result is described in Figure 7.8. Testing the linear velocity of end-effector, the motion is completely suppressed after $0.1\,[s]$ in both approaches, but the proposed one presents a large oscillation when the mass is high: the reason can be guessed in the high overshoot of force response that cause a large variation in arm position when the impact is detected. The same result is underline by kinetic energy response, where in Calculating Brake Time the energy converges to zero in $0.2355\,[s]$ instead of $0.2531[s]$ of KEDT when a small mass is used. The reaction force in end-effector domain has large overshoot in the proposed method caused by the important role of mass in kinetic energy. In both case, the worst situation happens when the nominal value coincides with the lowest one, because the system behaviour is the slowest.

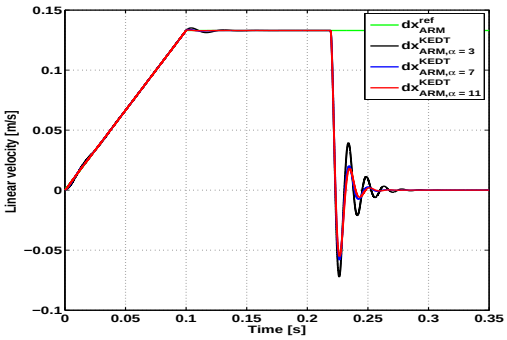

(a) KEDT, Arm Velocity Tracking in x-direction

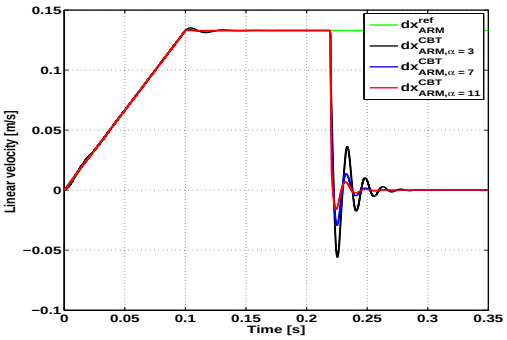

(b) CBT, Arm Velocity Tracking in x-direction

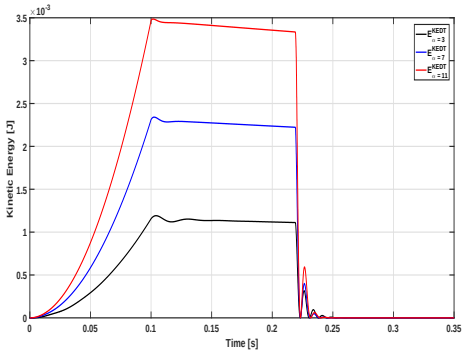

(c) KEDT, Kinetic Energy

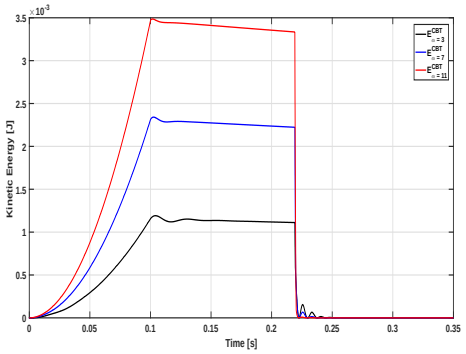

(d) CBT, Kinetic Energy

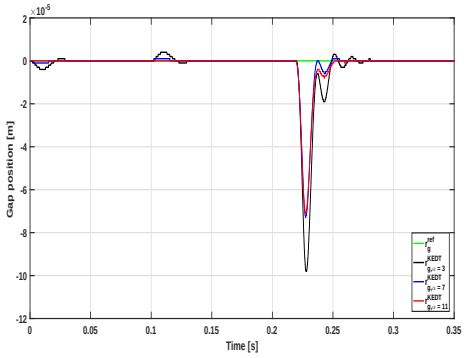

(e) KEDT, Gap Displacement

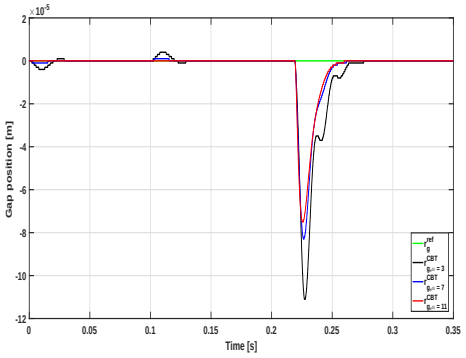

(f) CBT, Gap Displacement

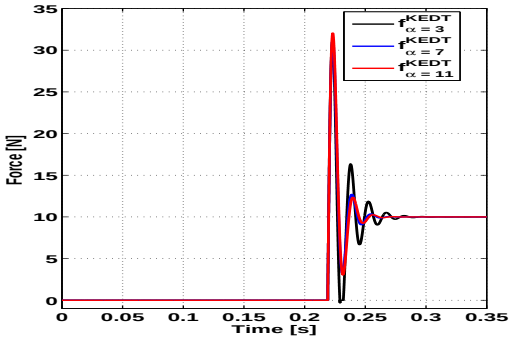

(g) KEDT, Reaction Force in x-direction

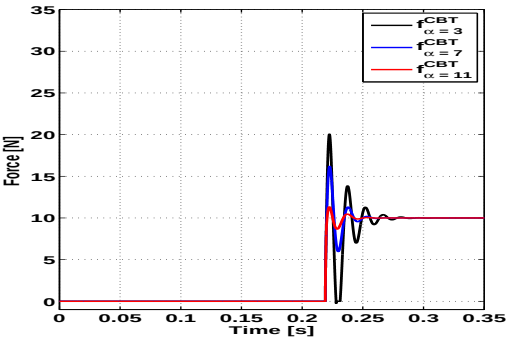

(h) CBT, Reaction Force in x-direction

Figure 7.8: One-link Manipulator, Contact Case

Parameter	*Character*	*Value*
Links Length	$L_1\, L_2\, L_3$	0.19, 0.095, 0.35 $[m]$
	$L_4\, L_5\, L_6$	$0.2, 0.08, 0.35$ $[m]$
Nominal Thrust Constant	K_{fn}	9.42 $[N/A]$
Nominal Torque Constant	$K_{\tau n}$	0.194 $[Nm/A]$
Nominal Magnetic Constant	K_{gn}	566000 $[N/m]$
Nominal Length of the Screw	l_p	$20 \cdot 10^{-3}$ $[m]$
Nominal Mass of the Mover	M_n	0.5 $[kg]$
Nominal Inertia of the Mover	J_n	$2 \cdot 10^{-3}$ $\left[kg \cdot m^2\right]$
Cut-off Frequency of Thrust Disturbance Observer	w_d	600 $[rad/s]$
Cut-off Frequency of Torque Disturbance Observer	$w_{d\tau}$	600 $[rad/s]$
Cut-off Frequency of Reaction Force Observer	w_{react}	600 $[rad/s]$
Proportional Gain of Gap Controller	K_{pg}	42925
Derivative Gain of Gap Controller	K_{dg}	410
Proportional Gain of Position Controller	K_{px}	1217
Derivative Gain of Position Controller	K_{dx}	67
Proportional Gain of Force Controller	K_{pf}	0.01
Derivative Gain of Force Controller	K_{df}	100

Table 7.4: Simulation Parameters of One-link and Two-link Manipulator

7.4 Two-link Manipulator

In this section only the SPM prototype is considered, the plant and control parameters used in simulation are shown in Table 7.4.
A trapezoidal move profile is applied for the creation of arm velocity reference. In this situation, the inputs signals are not affected by quantize noise in order to obtain results of easy understanding. The obstacle position is set different from motor starting point, as displayed in Figure 7.9

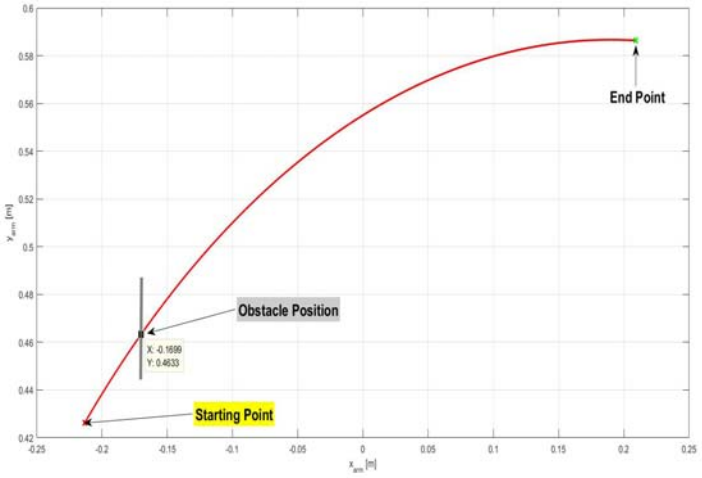

Figure 7.9: Two-link Manipulator, Obstacle Position

7.4.1 Contactless Case

The mass parameter is very important for trajectory tracking of robotic arm and when the nominal value coincides with the real one the system becomes unstable as show in Figure 7.10.
From the Equation (3.8) of parameter fluctuation model, a variation of $\alpha = 3$ and $\alpha = 11$ are performed in order to improve system stability. The arm tracking error is close to zero when a higher nominal value is used, especially in case of constant velocity. Regarding gap displacement, in the worst case, the oscillations are larger than in the first joint: it is due to the big linear position displacement and to the small value of mass matrix B(q).
Since large values of uncertain lead to better performances, in the further studies, $M_n = 6\,[Kg]$ ($\alpha = 11$) will be considered in order to perform a good analysis of inertia and magnetic constant fluctuations.
In Figure 7.11, $\alpha = |0.7|$ is applied to inertia nominal value. The variation does not affect the trajectory tracking, both in joint and end-effector domains. The q-axis current acquires high negative value when a position change occurs and α is 0.7: both inertia and I_q^{ref} current are related to rotary motion and a great value of current is required in order to guarantee the stability.
Finally, the nominal magnetic constant parameter is changed with uncertainty $\alpha = |0.7|$ in Figure 7.12. The variation does not influence the trajectory and reference velocity tracking, both in joint and end-effector domains. The variation of K_g does not interest system performance as nominal mass or inertia, because this parameter is not directly related to system output variables, like linear and rotary position, as the previous.
The above analysis reveals the importance of parameter fluctuation applied to the first joint: in this case the helical motor is subjected to inner variations and to ones given by the second joint. For this reason, motor one is more sensible to parameter variations than the second.

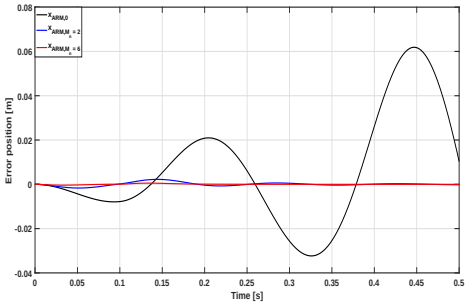

(a) Arm Trajectory Tracking Error in x-direction

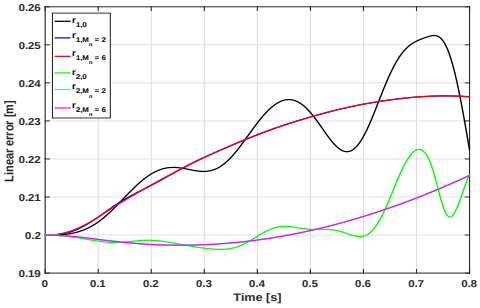

(b) Motor Trajectory Tracking

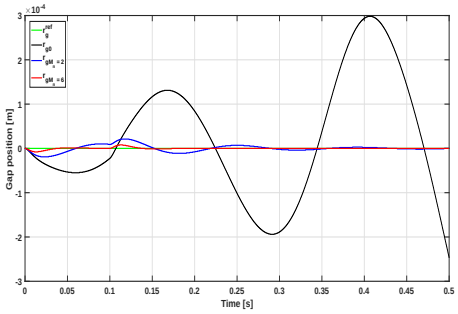

(c) Gap Displacement motor 1

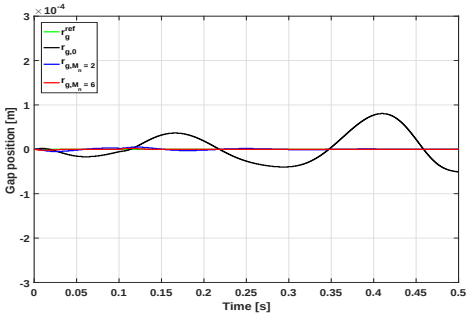

(d) Gap Displacement motor 2

Figure 7.10: Two-link Manipulator, Nominal Mass Variation

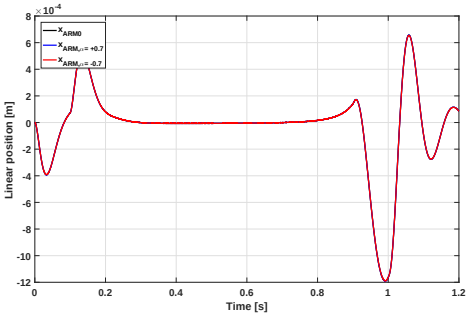

(a) Arm Trajectory Tracking Error in x-direction

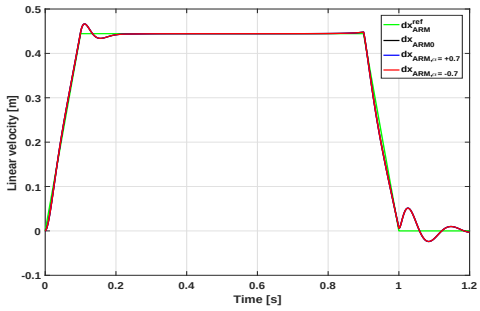

(b) Arm Velocity Tracking in x-direction

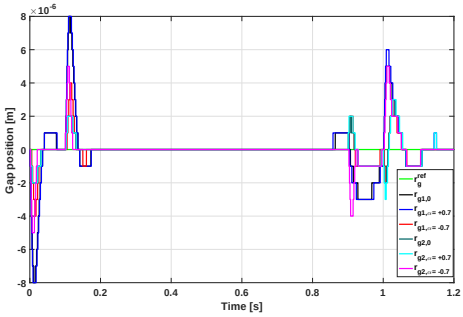

(c) Gap Displacement

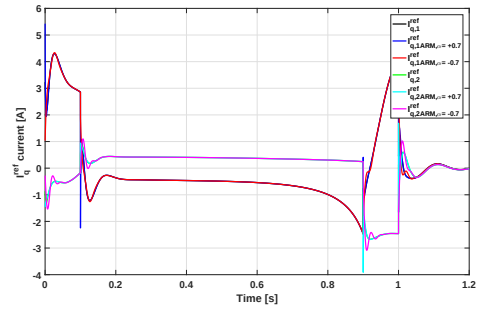

(d) I_q^{ref} Current

Figure 7.11: Two-link Manipulator, Nominal Inertia Variation

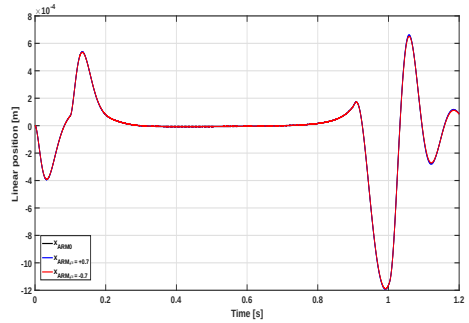

(a) Arm Trajectory Tracking Error in x-direction

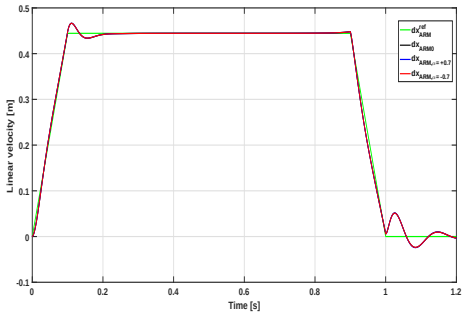

(b) Arm Velocity Tracking in x-direction

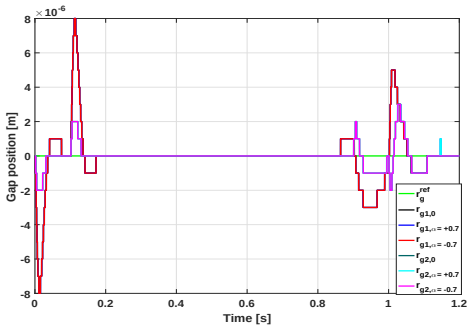

(c) Gap Displacement

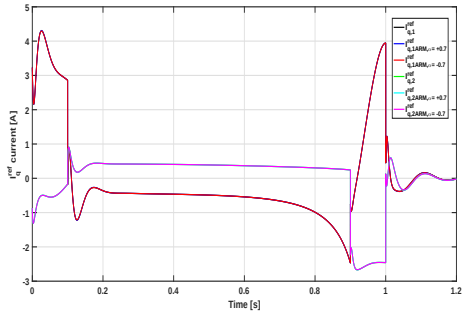

(d) I_q^{ref} Current

Figure 7.12: Two-link Manipulator, Nominal Magnetic Constant Variation

7.4.2 Contact Case

In this case the nominal mass is varied considering the uncertainty parameter α equal to 3, 7 and 11.
The results of the proposed method (KEDT) and of Calculating Brake Time (CBT) are compared. The suppression is applied to both joints: in this way, when the impact happen, all motors are controlled.
Figure 7.13 shows the simulation results and it can be seen that the two methods have close performance and the motion is suppressed in $0.15\,[s]$. The mainly difference appears in the kinetic energy of the second joint: even if in the proposed method are reached higher values, due to the different suppression approach, the energy converges to zero at the same time.

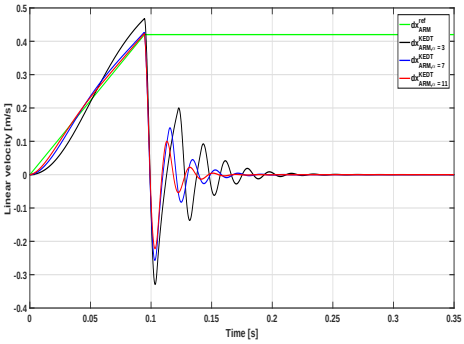

(a) KEDT, Arm Velocity in x-direction

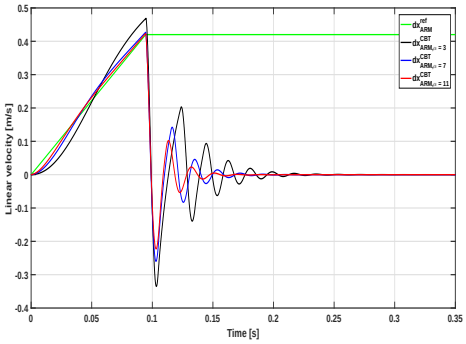

(b) CBT, Arm Velocity in x-direction

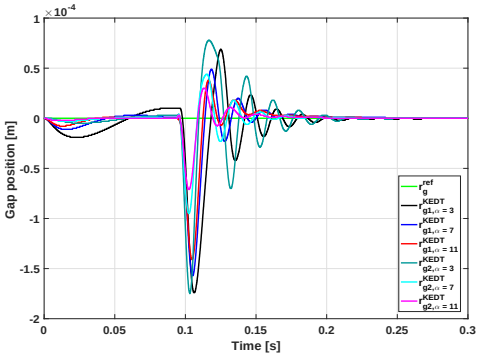

(c) KEDT, Gap Displacement

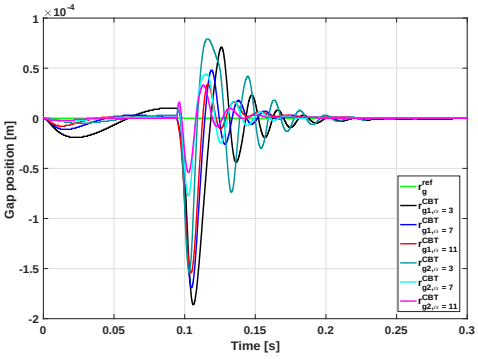

(d) CBT, Kinetic Energy motor 1

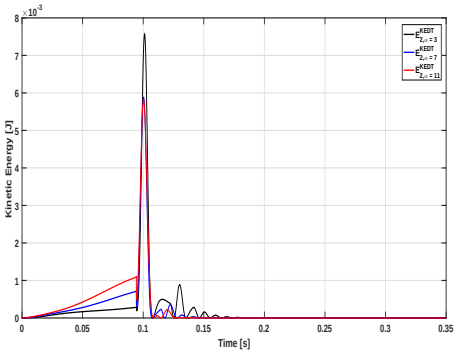

(e) KEDT, Kinetic Energy motor 2

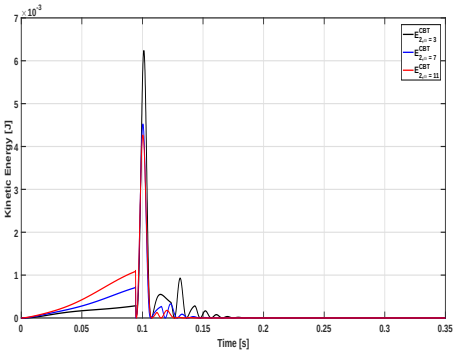

(f) CBT, Kinetic Energy motor 2

Figure 7.13: Two-link Manipulator, Contact Case

Chapter 8

Experiment

The results concerning helical motor obtained in simulation are verified considering only the IPM prototype. Two different situations are analysed: the contactless case and the contact one. In the first it is assumed no contact between the motor and obstacle, while the second considers the contact with an object and the performance of the proposed motion suppression method are analysed.

8.1 Experimental Set-up

The configuration of the experimental instruments and the block digram of its structure are shown in Figure 8.1. The IPM helical motor is considered and the DSP is implemented by the My Way Engineering Co., Ltd. In particular the PE - Expert 3 is provided as the computing unit: it is a power electronics control system equipped with a high-performance DSP whose clock frequency is $225\,[MHz]$. The specification of each experimental components is described in Table 8.1.
Furthermore, an elastomer implements the hard obstacle which is set at $0.009\,[m]$ from the motor end-effector, as display in Figure 8.2.

Component	*Specification*	*Value*
DSP : PE - Expert 3	Dead time	20 $[ns]$- 10.22 $[\mu s]$
	Carrier frequency	10 $[Hz]$- 200 $[kHz]$(3 phase PWM)
Inverter : MWINV-4R222	Rated output capacity	4.2 $[kVA]$
	Rated output current	11 $[A]$
	Rated output voltage	$0 - 220V$ $[V]$
Linear encoder : RGH24X30D00A	Resolution	1 $[\mu s]$
Rotary encoder : MG-30	Resolution	2/20000 $[rad]$

Table 8.1: Experiment Specifications

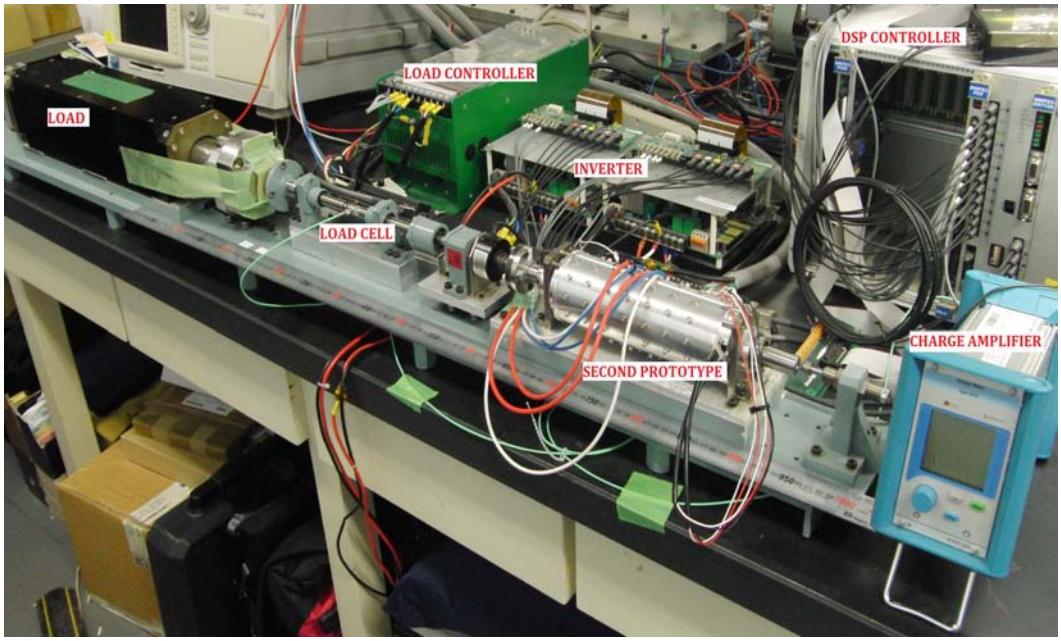

(a) Experiment Environment

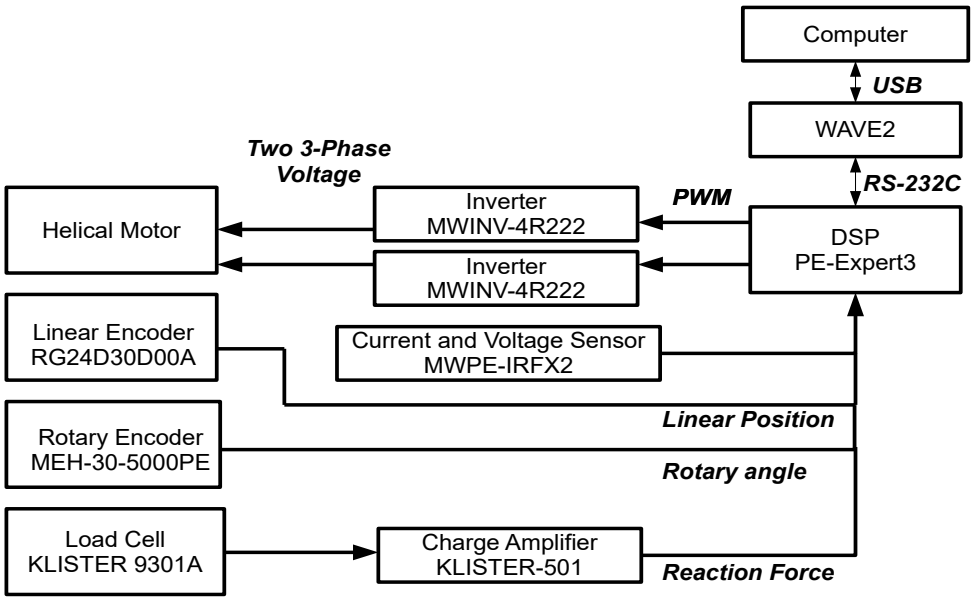

(b) Structure of Experimental Equipment

Figure 8.1: Experiment Environment

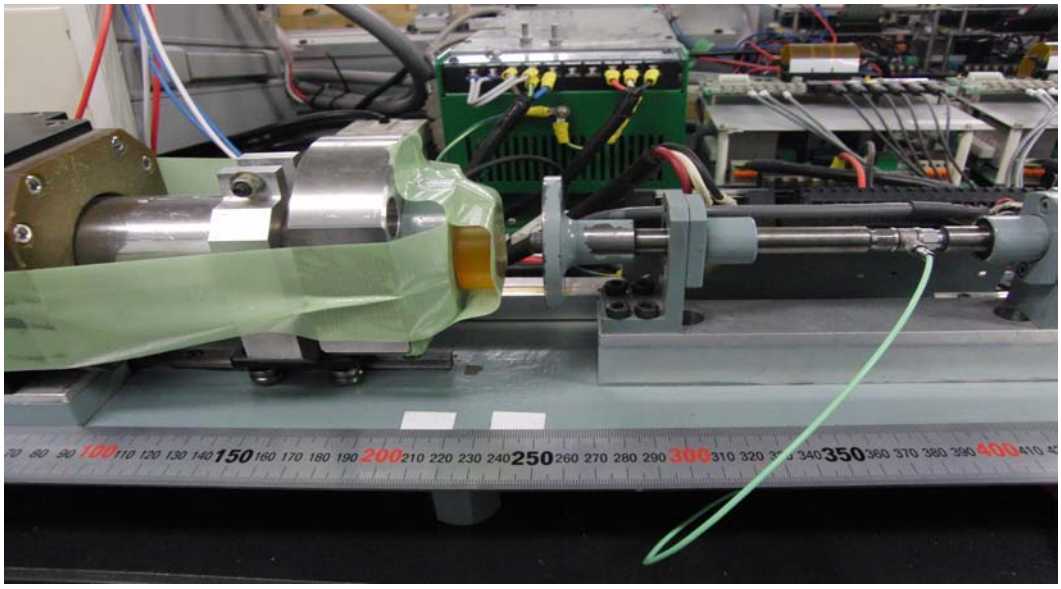

(a) Experiment Environment, Obstacle

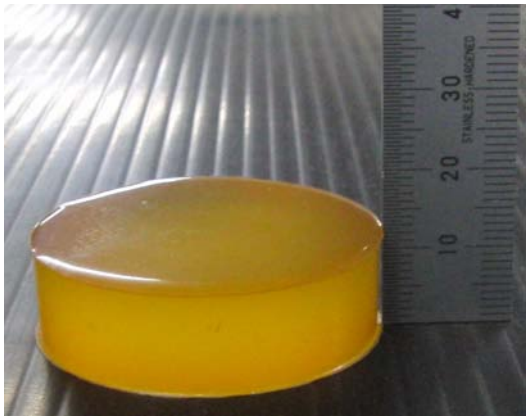

(b) Elastomer, Frontal View

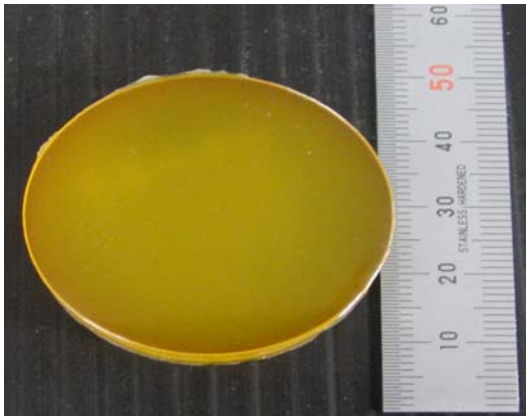

(c) Elastomer, Top View

Figure 8.2: Contact Environment

8.2 Experiment Results

In this section, the IPM prototype is considered and its plant and control parameters are shown in Table 8.2: the model coincides with the one considered in simulation, while control gains are chosen suited to the experimental set-up.
Concerning the contact case an elastomer implements the hard obstacle and it is placed in front of the motor. Furthermore, the achievements is compared with a method for impact force suppression, the Calculating Brake Time (CBT).

Parameter	*Character*	*Value*
Nominal Thrust Constant	K_{fn}	11.15 $[N/A]$
Nominal Torque Constant	$K_{\tau n}$	0.105 $[Nm/A]$
Nominal Magnetic Constant	K_{gn}	122000 $[N/m]$
Nominal Length of the Screw	l_p	$22 \cdot 10^{-3}$ $[m]$
Nominal Mass of the Mover	M_n	0.7 $[kg]$
Nominal Inertia of the Mover	J_n	$1.26 \cdot 10^{-4}$ $[kg \cdot m^2]$
Cut-off frequency of Torque Disturbance Observer	$w_{d\tau}$	500 $[rad/s]$
Cut-off frequency of Reaction Force Observer	w_{react}	500 $[rad/s]$
Cut-off frequency of Low Pass Filter Pseudo-Derivative	w_{diff}	3000 $[rad/s]$
Cut-off frequency of Kinetic Energy Pseudo-Derivative	w_E	400 $[rad/s]$
Proportional Gain of Gap Controller	K_{pg}	25600
Derivative Gain of Gap Controller	K_{dg}	320
Proportional Gain of Position Controller	K_{px}	8100
Derivative Gain of Position Controller	K_{dx}	180
Proportional Gain of Force Controller	K_{pf}	0.1
Damping gain of Force Controller	K_{df}	0
Cut-off frequency of Thrust Disturbance Observer	w_d	500 $[rad/s]$
Sampling Period of Controller	T_s	83.3 $[\mu s]$
Resolution of Linear Encoder	$-$	1 $[\mu s]$
Resolution of Rotary Encoder	$-$	$4 \times 5000\,[pulse/r]$
Limit q-axis Current	I_q^{lim}	8 $[A]$
Limit d-axis Current	I_d^{lim}	12 $[A]$
Gap Power Threshold	$\Delta \mathrm{L}_{thr}$	0.09 $[W]$

Table 8.2: Experiment Parameters

8.2.1 Contactless Case

In this section, the results are shown in Figure 8.3. Even if experimental system is more sensible to parameter values, the simulation results of mass and magnetic force constant variations are confirmed: according to Section 7.2, lower values of mass produce higher tracking error for gap and position displacement. Moreover, the real system is still robust to K_g and its variation causes smaller changes.
Increasing inertia, the current values change with high frequency, especially when the velocity is constant, as suggested in Section 7.2 and the controlled variables, x_g and x, become unstable. For this reason the experiment is conducted using $\alpha = |0.2|$.

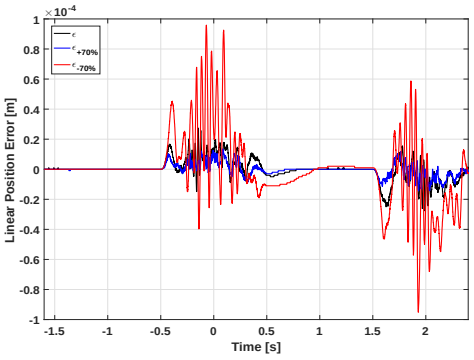

(a) Position Error, Mass Variation

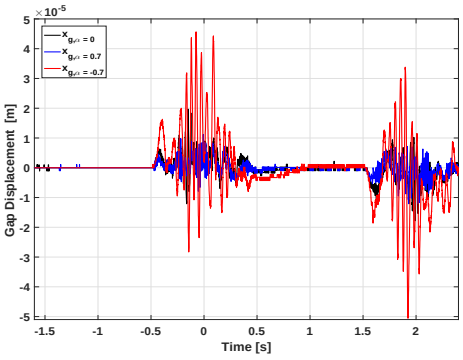

(b) Gap Displacement, Mass Variation

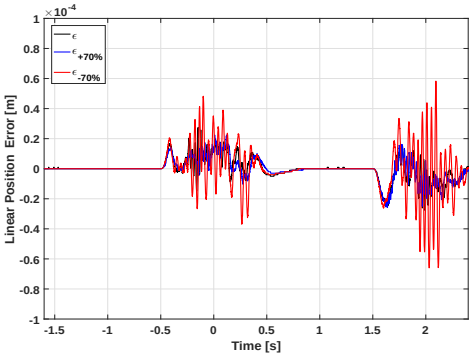

(c) Position Error, Magnetic Constant Variation

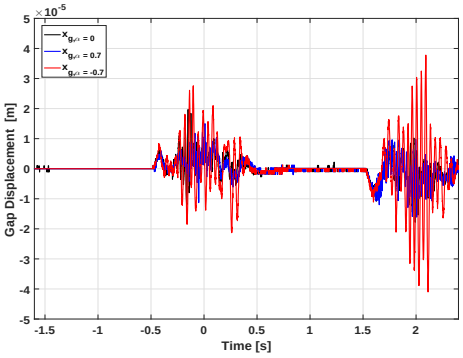

(d) Gap Displacement, Magnetic Constant Variation

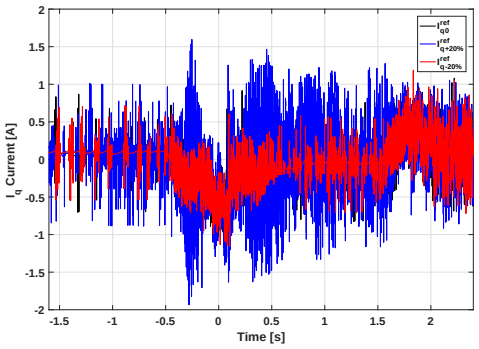

(e) I_q^{ref} current, Inertia Variation

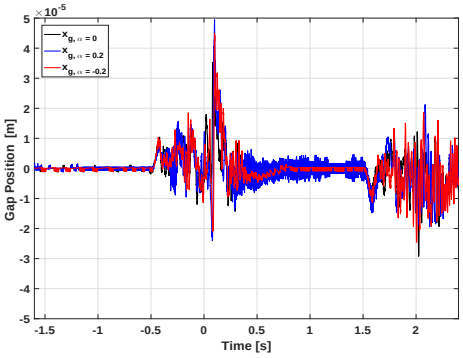

(f) Gap Displacement, Inertia Variation

Figure 8.3: IPM Prototype, Experimental Results for Contactless Case

8.2.2 Contact Case

In this section, the performance of motion suppression methods are tested.
The impact is detected when the gap power is more than a prefixed threshold, sets at $0.09\,[W]$ for all cases. This value is higher than the one used in simulation because of the disturbances introduced by the real motor. The time motion from zero to $0.01\,[m]$ is set at $0.2\,[s]$ in order to analyse the case of high velocity impact.
In Table 8.3 the Root Mean Square of kinetic energy for each experiment is com-

puted. All variation are performed four times, in order to improve the reliability of results. The evaluated function considers the samples from the impact detection: in this case, the energy before the contact is neglected. High variations lead to high kinetic energy because of the mass value. The results confirmed the repeatability of experiment and validate the accuracy of both methods.
Figure 8.4 shows the kinetic energy, force, linear velocity and position for α equal to -0.5, 0 and 0.5 respectively, related to sets with the closest root mean square value.
The behaviour with smaller variation are similar in the two approaches as in simulation. The kinetic energy is lower in the the proposed method for $\alpha = 0.5$ and the linear velocity has a little overshoot as get in Section 7.2. The best performance is given by lower mass value: the force peak is small and the suppression acts immediately in both cases.
Related the robustness of parameter fluctuation, is not possible determine which approach is better, because the results are very close, especially for α equal to -0.5 and 0. On the other hand, the proposed method is robust to mass uncertainty because the variation of the responses obtained in each cases is similar.

$Variation$	$Methods$	
	CBT	$KEDT$
$\alpha = -0.5$	$1.1366 \cdot 10^{-4}$	$2.9608 \cdot 10^{-5}$
	$3.6298 \cdot 10^{-5}$	$2.2400 \cdot 10^{-5}$
	$3.6298 \cdot 10^{-5}$	$3.2242 \cdot 10^{-5}$
	$4.2833 \cdot 10^{-5}$	$2.4127 \cdot 10^{-5}$
$Mean$	$5.7271 \cdot 10^{-5}$	$2.7094 \cdot 10^{-5}$
$\alpha = 0$	$7.0749 \cdot 10^{-5}$	$6.8701 \cdot 10^{-5}$
	$5.6044 \cdot 10^{-5}$	$5.8754 \cdot 10^{-5}$
	$6.4526 \cdot 10^{-5}$	$7.0224 \cdot 10^{-5}$
	$6.8625 \cdot 10^{-5}$	$6.6351 \cdot 10^{-5}$
$Mean$	$6.4986 \cdot 10^{-5}$	$6.6007 \cdot 10^{-5}$
$\alpha = 0.5$	$8.6887 \cdot 10^{-5}$	$8.2590 \cdot 10^{-5}$
	$1.0641 \cdot 10^{-4}$	$1.1151 \cdot 10^{-4}$
	$1.2791 \cdot 10^{-4}$	$1.3218 \cdot 10^{-4}$
	$1.0467 \cdot 10^{-4}$	$1.1835 \cdot 10^{-4}$
$Mean$	$1.0647 \cdot 10^{-4}$	$1.1116 \cdot 10^{-4}$

Table 8.3: Root Mean Square of Kinetic Energy

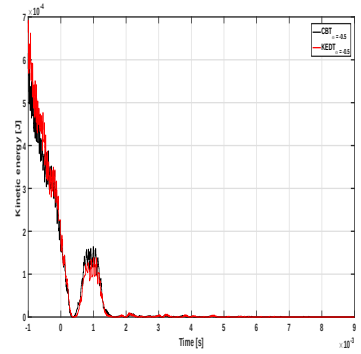

(a) Kinetic Energy, $\alpha = -0.5$

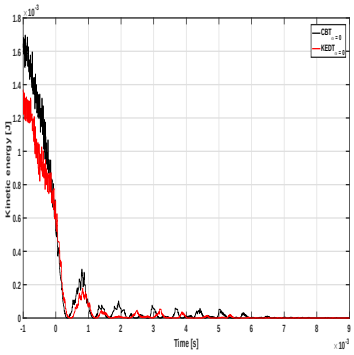

(b) Kinetic Energy, $\alpha = 0$

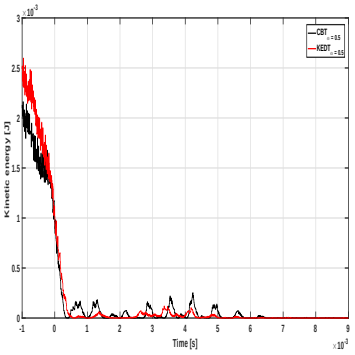

(c) Kinetic Energy, $\alpha = +0.5$

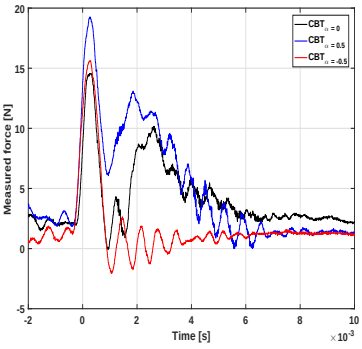

(d) Impact Force, CBT

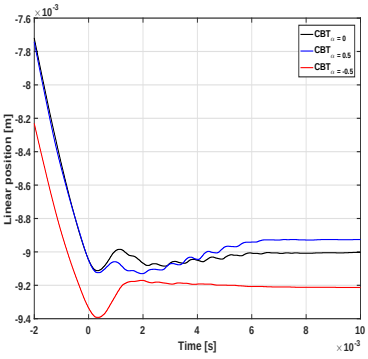

(e) Linear Position, CBT

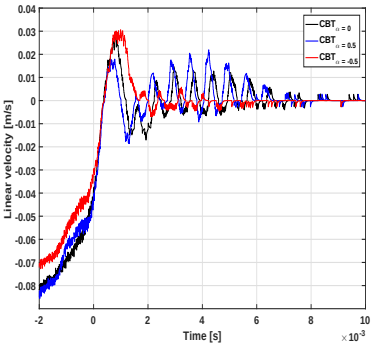

(f) Linear Velocity, CBT

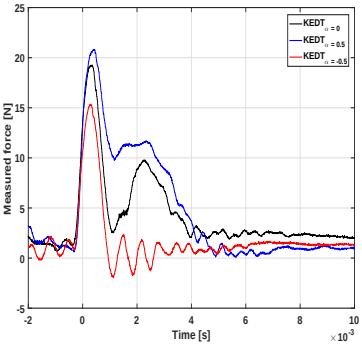

(g) Impact Force, KEDT

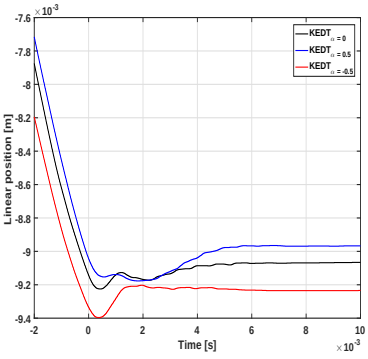

(h) Linear Position, KEDT

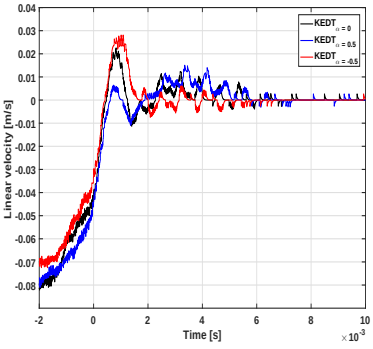

(i) Linear Velocity, KEDT

Figure 8.4: Experimental Results of Contact Case

Chapter 9

Conclusion

The analysis of robustness to parameter fluctuation for helical motors is performed in different situations. The contactless case is tested as well as the contact one, where the validity of proposed approach for motion suppression, called Kinetic Energy Derivative Threshold, is compared with an existing method, called Calculating Brake Time.
Furthermore, mathematical models of one and two link manipulators are derived in order to test robustness of the SPM spiral motor as applied joint.
For each situation the simulation results are analysed and only the performance of IPM helical motor is tested in experiment.
In chapter 7, Section 7.2, two different prototypes of helical motor are used. Regarding IPM motor, inertia and magnetic constant do not influence the trajectory tracking as the mass variation does: higher value of mass lead to better performance. Moreover, the system results to be sensible to high inertia values that causes important oscillations to I_q^{ref} current. Good results are obtained for K_g variation.
The work is extended to the SPM prototype and the result confirms the previous achievement: higher mass parameter values are more advisable. By using the same control gain values, the IPM prototype can resist to an higher parameter uncertainties.
Concerning the motion suppression, small values of mass lead to the same results while, with high value, the velocity converges to zero faster in Kinetic Energy Derivative Threshold.
In Section 7.3 the behaviour of SPM helical motor applied as joint to one-link manipulator is analysed. Since the mass matrix depends on the posture, the acceleration control system tends to be unstable: it can be avoid by acting on nominal mass in order to design the nominal mass matrix higher. Moreover, the inertia influences I_q^{ref} current, especially when the velocity is not constant. The Kinetic Energy Derivative Threshold has important oscillations in velocity and kinetic energy response, but the motion is suppressed at the same time of Calculating Brake Time approach.
In Section 7.4 the first joint of the two-link robotic arm is more sensible to parameter fluctuations because of the second helical motor placed near its end.
In Chapter 8 the performance of IPM spiral motor are tested. Even if the real system is more sensitive to parameter changing, the simulation achievements about nominal mass, inertia and magnetic constant are confirmed. In this situation, an

upper bound for inertia variations has to be fixed, otherwise the acceleration control system becomes unstable.
The experiment shows that Kinetic Energy Derivative Threshold is robust to parameter fluctuation and all kinetic energy is consumed after the collision.

Appendices

Appendix A

Disturbance Observer

The Disturbance Observer (DOB) is used in the motion-control field to suppress disturbances (such as external force, error model,...) or to make a closed-loop system stable. K. Ohnishi introduced it to estimate disturbances from model information [16]. Because of its simple structure[17] and its easy understanding, the DOB is used in many applications and it can be applied on nonlinear models.

A.1 Problem Formulation

Consider the system described by:

$$\begin{cases} \dot{x}(t) = Ax(t) + Bu(t) \\ y(t) = Cx(t) + d(t) \end{cases}$$

where $x \in \mathbb{R}^n$ is the state variable, $u \in \mathbb{R}^p$ is the control input, $y \in \mathbb{R}^m$ is the system output, $d \in \mathbb{R}^m$ is the disturbance, $A \in \mathbb{R}^{n \times n}$, $B \in \mathbb{R}^{n \times p}$ and $C \in \mathbb{R}^{m \times n}$. Assuming (C,A) detectable and (A,B) stabilizable, the transfer function between input and output is:

$$W(s) = C(sI - A)^{-1}B,\ W(s) \in \mathbb{R}^{m \times p}. \tag{A.1}$$

Supposing that $u(t)$ and $y(t)$ are available but the disturbance $d(t)$ is unavailable, the disturbance observer as disturbance estimator is used. The estimation is based on the measurement of the input and the output and the general form of the disturbance observer is written as:

$$\hat{d}(s) = G_1(s)y(s) + G_2(s)u(s). \tag{A.2}$$

where $\hat{d}(s) = \mathcal{L}(\tilde{d}(t))$[1], $\hat{d}(t) \in \mathbb{R}^m$, $G_1 \in \mathbb{R}^{m \times m}$ and $G_2 \in \mathbb{R}^{m \times p}$. Then, $\hat{d}(s)$ is a disturbance observer for any disturbance if, for any $x(0)$, $u(t)$ and $d(t)$, is satisfied:

$$\lim_{t \to \infty} \left(d(t) - \hat{d}(t) \right) = 0. \tag{A.3}$$

[1]The symbol $\mathcal{L}(\cdot)$ indicates the Laplace operator.

Appendix B

Mathematical Model of Helical Motor

B.1 Magnetic Circuit and Circuit Equations

In the spiral motor, the radial direction is supported by a linear bush and the axial force is controlled by the electromagnetic force of the coil winding and the magnet of the mover. In this case, the mover is attracted to the stator by the attractive force acting between the stator and the mover magnet (uncontrolled state). For this reason an appropriate current is applied to the winding in order to perform the magnetic levitation control and the air gap x_g is kept constant between the stator and the mover. In Figure B.1(a), the relationship between the axial position x and the rotation angle θ is described. The case of uncontrolled state is represented in Figure B.1(b): at the time of the magnetic levitation control, the mover is separated from the stator and it is floating in the horizontal direction; otherwise the stator and the mover are in contact one with the other.
The air gap displacement is related to linear and rotary motion by the following relation

$$x_g = x - \frac{l_p}{2\pi}\theta. \tag{B.1}$$

In Figure B.2 is described the layout of polar coordinates expression of the motor and the equivalent magnetic circuit for a SPM prototype, where $R_g = \frac{3p(l_g - x_g)}{S\mu_0}$ is the magnetic resistance of the front part of air gap of each phase, $R'_g = \frac{3p(l_g + x_g)}{S\mu 0}$ is the magnetic resistance of the back part[1] and $R_m = \frac{3pl_m}{S\mu_m}$ is the magnetic resistance of the permanent magnet. The quantity $c(\theta)I_f$ is a spatial function of magnetomotive force caused by the permanent magnet and dependent on the overlapping angle between the permanent magnet and the winding. Through fundamental wave component of Fourier series expansion, it can be approximated by a cosine function $c(\theta) = k\cos(\theta)$, where $k = \frac{6\sqrt{3}}{\pi^2}$. Furthermore, $I_f = B_r\frac{l_m}{\mu_m}$ indicates the equivalent magnetization current of the permanent magnet of the front gap, I'_f is the magnetization current of the back gap, μ_0 and μ_m is the permeability in the vacuum and

[1] In order to distinguish the front and the back side, an apostrophe (') is added to the parameter relating to the back side.

in the permanent magnet respectively[2].
The nomenclature and the values of motor parameters are shown in Table B.1 and B.2.

Parameter	*Description*
B_r	Residual flux density
f	Thrust force of the mover
I_i	i-axis current on forward side windings
I_i'	i-axis current on backward side windings
I_f	Magnetization current of the permanent magnet
J	Moment of inertia of the mover around the axis
k	Fundamental Fourier component of $c(\theta)$
l_g	Nominal length of gap
l_m	Thickness of magnet
l_p	Lead length of the screw
M	Mass of the mover
n	Number of turns of windings
p	Number of pole pairs
q	Number of mover layers
S	Gap area of cross section
τ	Torque of the mover
x	Linear position of the mover
x_g	Gap displacement
θ	Rotary position of the mover

Table B.1: Nomenclature

[2] For simplicity, it is assumed that the permeability in the permanent magnet μ_m coincides with the one in the vacuum μ_0.

Parameter	*Description*	*Value*
B_r	Residual flux density	1.21 $[T]$
l_g	Nominal length of gap	1.0 $[mm]$
n	Number of turns of windings	50
p	Number of pole pairs	2
q	Number of mover layers	4
S	Gap area of cross section	907.9 $[mm^2]$
–	Number of stator layers	6

Table B.2: Parameters of Helical Motor

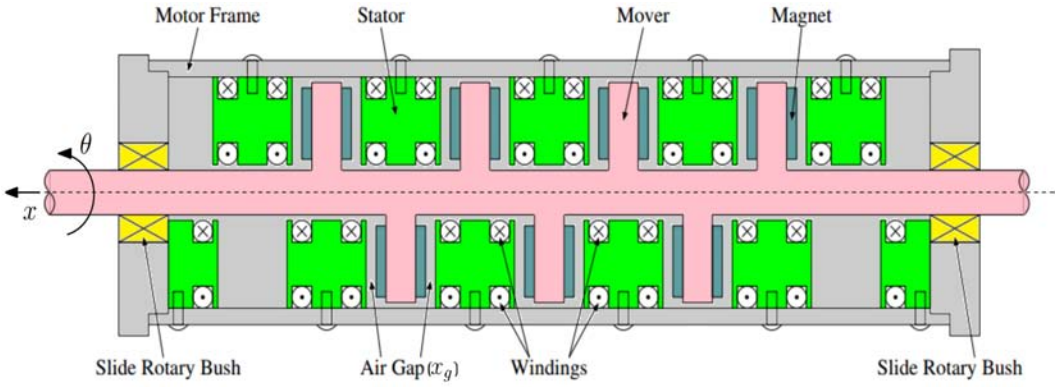

(a) Cross-sectional View

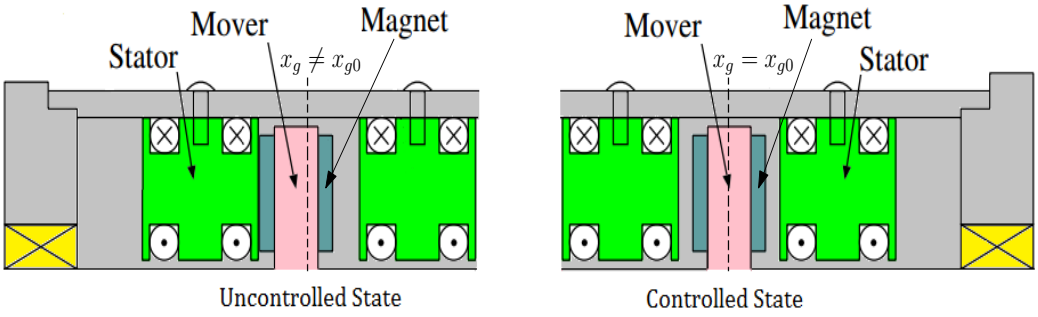

(b) Magnetic Levitation Control

Figure B.1: Spiral Motor Structure

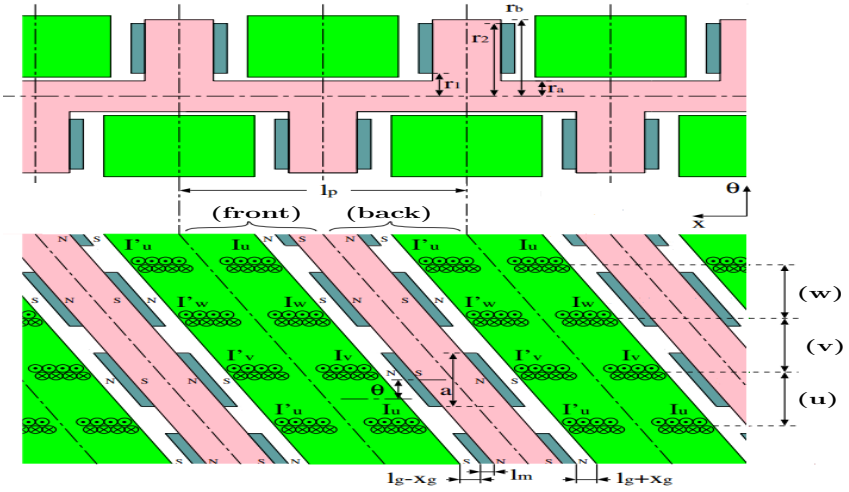

(a) Helical Motor in Polar Coordinates

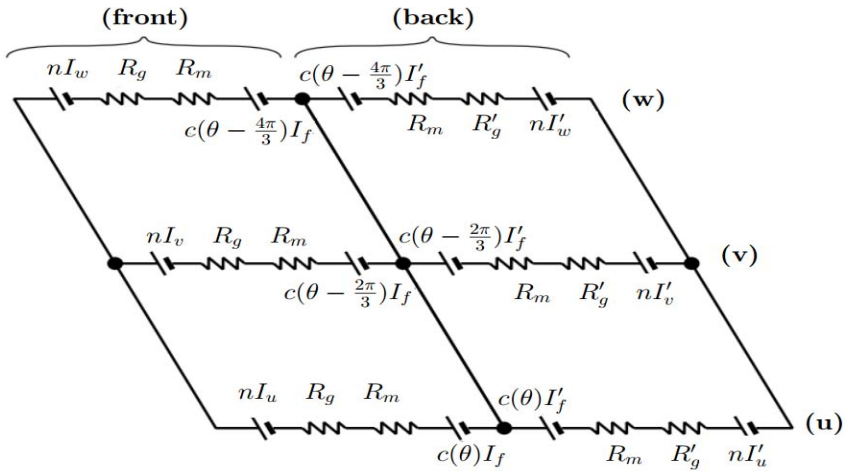

(b) Magnetic Circuit of Helical Motor

Figure B.2: Spiral Motor in Polar Coordinates and the Equivalent Magnetic Circuit

Considering the front side of the magnetic circuit in Figure B.2, the total interlinkage flux $\Phi = [\Phi_u, \Phi_v, \Phi_w, \Phi_m]^T$ for each current is defined as $\Phi = LI$, where $I = [I_u, I_v, I_w, I_m]^T$ is the current vector and L is the inductance matrix:

$$L = P \begin{bmatrix} n^2 & -\frac{n^2}{2} & -\frac{n^2}{2} & \frac{3}{2}knc_0 \\ -\frac{n^2}{2} & n^2 & -\frac{n^2}{2} & \frac{3}{2}knc_1 \\ -\frac{n^2}{2} & -\frac{n^2}{2} & n^2 & \frac{3}{2}knc_2 \\ \frac{3}{2}knc_0 & \frac{3}{2}knc_1 & \frac{3}{2}knc_2 & \left(\frac{3k}{2}\right)^2 \end{bmatrix}. \tag{B.2}$$

Here, $P = \frac{2}{3(R_g+R_m)}$ is the permeance for one-phase current and $c_i = \cos\left(p\theta - \frac{2\pi}{3}i\right)$. Defining the voltage vector $V = [V_u, V_v, V_w, V_f]^T$ of each windings, the voltage equations of the spiral motor are:

$$V = RI + L\frac{dI}{dt} + \dot{\theta}\frac{\partial L}{\partial \theta}I + \dot{x}\frac{\partial L}{\partial x}I \tag{B.3}$$

In order to apply a field oriented control to the spiral motor, the dq-axis model

has to be derived. From the conversion matrix from three phases to two phases C_c and the transformation matrix from a stationary coordinate system to a rotating coordinate system C_t, the transformation matrix C to dq coordinates is expressed as follows.

$$C_c = \begin{bmatrix} \sqrt{\frac{2}{3}}\cos(0) & \sqrt{\frac{2}{3}}\cos(\frac{2}{3}\pi) & \sqrt{\frac{2}{3}}\cos(\frac{4}{3}\pi) & 0 \\ \sqrt{\frac{2}{3}}\sin(0) & \sqrt{\frac{2}{3}}\sin(\frac{2}{3}\pi) & \sqrt{\frac{2}{3}}\sin(\frac{4}{3}\pi) & 0 \\ \frac{1}{\sqrt{3}} & \frac{1}{\sqrt{3}} & \frac{1}{\sqrt{3}} & 0 \\ 0 & 0 & 0 & 1 \end{bmatrix} \tag{B.4}$$

$$C_t = \begin{bmatrix} \cos(p\theta) & \sin(p\theta) & 0 & 0 \\ -\sin(p\theta) & \cos(p\theta) & 0 & 0 \\ 0 & 0 & 1 & 0 \\ 0 & 0 & 0 & 1 \end{bmatrix} \tag{B.5}$$

$$C = C_c C_t = \begin{bmatrix} \sqrt{\frac{2}{3}}c_0 & \sqrt{\frac{2}{3}}c_1 & \sqrt{\frac{2}{3}}c_2 & 0 \\ -\sqrt{\frac{2}{3}}s_0 & -\sqrt{\frac{2}{3}}s_1 & -\sqrt{\frac{2}{3}}s_2 & 0 \\ \frac{1}{\sqrt{3}} & \frac{1}{\sqrt{3}} & \frac{1}{\sqrt{3}} & 0 \\ 0 & 0 & 0 & 1 \end{bmatrix} \tag{B.6}$$

where $s_i = \sin\left(p\theta - \frac{2\pi}{3}i\right)$.
Then, the dq-axis current and voltage are represented by the follows equation:

$$I_{dq} = [I_d, I_q, I_0, I_f]^T = CI \tag{B.7}$$

$$\begin{aligned} V_{dq} &= [V_d, V_q, V_0, V_f]^T = CV = CRC^T I_{dq} + CLC^T \dot{I}_{dq} \\ &+ \dot{\theta} C \frac{\partial L}{\partial \theta} C^T I_{dq} \dot{\theta} C L \frac{\partial C^T}{\partial \theta} I_{dq} + \dot{x} C \frac{\partial L}{\partial x} C^T I_{dq} \end{aligned} \tag{B.8}$$

where the subscript d, q and 0 are related to d-axis, q-axis and zero-phase values, respectively.
Finally, the dq-axis voltage equations for the front and back part are described in (B.9) and (B.10).

$$\begin{aligned} \begin{bmatrix} V_d \\ V_q \end{bmatrix} &= \begin{bmatrix} R + L_d\left(\frac{d}{dt}\right) & 0 \\ 0 & R + L_q\left(\frac{d}{dt}\right) \end{bmatrix} \begin{bmatrix} I_d \\ I_q \end{bmatrix} + \Phi \begin{bmatrix} \frac{\dot{x}_g}{l - x_g} \\ p\theta \end{bmatrix} \\ &+ \frac{\dot{x}_g}{l - x_g} \begin{bmatrix} L_d & 0 \\ 0 & L_q \end{bmatrix} \begin{bmatrix} I_d \\ I_q \end{bmatrix} + p\dot{\theta} \begin{bmatrix} 0 & -L_q \\ L_d & 0 \end{bmatrix} \begin{bmatrix} I_d \\ I_q \end{bmatrix} \end{aligned} \tag{B.9}$$

$$\begin{aligned} \begin{bmatrix} V'_d \\ V'_q \end{bmatrix} &= \begin{bmatrix} R + L'_d\left(\frac{d}{dt}\right) & 0 \\ 0 & R + L'_q\left(\frac{d}{dt}\right) \end{bmatrix} \begin{bmatrix} I'_d \\ I'_q \end{bmatrix} + \Phi' \begin{bmatrix} \frac{\dot{x}_g}{l - x_g} \\ p\theta \end{bmatrix} \\ &+ \frac{\dot{x}_g}{l - x_g} \begin{bmatrix} L'_d & 0 \\ 0 & L'_q \end{bmatrix} \begin{bmatrix} I'_d \\ I'_q \end{bmatrix} + p\dot{\theta} \begin{bmatrix} 0 & -L'_q \\ L'_d & 0 \end{bmatrix} \begin{bmatrix} I'_d \\ I'_q \end{bmatrix} \end{aligned} \tag{B.10}$$

Here, Φ is the field flux of permanent magnet, L_q and L_d are the dq-axis inductance, $l = l_g + l_m$ is the gap length and R is the winding resistance.

B.2 Equations of Motion

The thrust f and the torque τ generated by the motor are obtained from the forward and backward part:

$$\begin{aligned} f &= \frac{1}{2} I_{dq}^T C \frac{\partial L}{\partial x} C^T I_{dq} \\ &= \frac{1}{l - x_g} \left(\Phi_f I_d \frac{1}{2} \left(L_d I_d^2 + L_q I_q^2 + L_f I_f^2 \right) \right) \qquad \text{(B.11)} \\ f' &= \frac{1}{l - x_g} \left(\Phi'_f I'_d \frac{1}{2} \left(L'_d I'^2_d + L'_q I'^2_q + L'_f I'^2_f \right) \right) \qquad \text{(B.12)} \\ \tau &= \frac{1}{2} I_{dq}^T C \frac{\partial L}{\partial \theta} C^T I_{dq} \\ &= p \Phi_f I_q + p(L_d - L_q) I_d I_q \\ &\quad - \frac{l_p}{2\pi} \frac{1}{l - x_g} \left(\Phi_f I_d \frac{1}{2} \left(L_d I_d^2 + L_q I_q^2 + L_f I_f^2 \right) \right) \qquad \text{(B.13)} \\ \tau' &= p \Phi'_f I'_q + p(L'_d - L'_q) I'_d I'_q \\ &\quad - \frac{l_p}{2\pi} \frac{1}{l - x_g} \left(\Phi'_f I'_d \frac{1}{2} \left(L'_d I'^2_d + L'_q I'^2_q + L'_f I'^2_f \right) \right). \qquad \text{(B.14)} \end{aligned}$$

Defining the total thrust f_{tot} and torque τ_{tot} of the spiral motor, the equations of motion in linear and rotary directions are described in (B.17) and (B.18).

$$\begin{aligned} f_{tot} &= pq(f + f') \qquad \text{(B.15)} \\ \tau_{tot} &= pq(\tau + \tau') \qquad \text{(B.16)} \\ M\ddot{x} &= f_{tot} - D_f \dot{x} - d_f \qquad \text{(B.17)} \\ J\ddot{\theta} &= \tau_{tot} - D_\tau \theta - d_\tau \qquad \text{(B.18)} \end{aligned}$$

where D_f, D_τ are the friction coefficients for linear and rotary motion, respectively, and d_f, d_τ are external force and torque applied to the mover.

B.3 Linear Approximation Motion Model

The control system of helical motor is based on the linear approximation model of equations (B.11)-(B.14): the Taylor expansion around $x_g = 0$ is applied and only the first order coefficient is extracted.
It is supposed that the dq-axis currents are current-controlled so that $I_d = -I'_d$ and $I_q = I'_q$. Furthermore, it is introduced the suffix "0" to indicate the parameter value around $x_g = 0$.
Finally, the the torque constant K_τ, the thrust constant K_f and the magnetic attraction force constant K_g are defined.

$$f_{tot} = pq\left(\frac{2L_{f0}I_f^2 x_g}{l^2 - x_g^2} + \frac{2l\Phi_{f0}I_d}{l^2 - x_g^2}\right) \tag{B.19}$$

$$\simeq \left(\frac{2pqL_{f0}I_f^2}{l^2}\right)x_g + \left(\frac{2pq\Phi_{f0}}{l}\right)I_d \tag{B.20}$$

$$= K_g x_g + K_f I_d \tag{B.21}$$

$$\tau_{tot} \simeq \left(2p^2 q\Phi_{f0}\right)I_q - \frac{l_p}{2\pi}f_{tot} \tag{B.22}$$

$$= K_\tau I_q - \frac{l_p}{2\pi}\left(K_g x_g + K_f I_d\right). \tag{B.23}$$

The motion model is written through the linear approximate motion equations of the helical motor:

$$M\ddot{x} = K_g x_g + K_f I_d - d_f \tag{B.24}$$

$$J\ddot{\theta} = K_\tau I_q - \frac{l_p}{2\pi}\left(K_g x_g + K_f I_d\right) - d_\tau. \tag{B.25}$$

Appendix C

Types of Helical Motor

The helical motor is a linear actuator that converts rotational motion into linear motion. It has a spiral structure for both the mover and the stator, two systems of three phase windings are arranged on the stator side and permanent magnets are located on the mover side. Since it has a helical structure, the area where the stator faces the mover is larger, the magnetic flux can be utilized with high density and high thrust can be obtained.
Two different types of spiral motor are developed, the Interior Permanent Magnet (IPM) and the Surface-mounted Permanent Magnet (SPM).

C.1 Interior Permanent Magnet (IPM)

The IPM motor is characterized by the location of the permanent magnet that is embedded in a slot provided in the mover. High precision helical curved surface is realized and the mechanical strength is significant. Moreover, both the mover and the stator, shown in Figure C.1(a), are made of silicon steel. Furthermore, since the magnet is embedded so as not to move, it makes possible to protect the magnet from impact and is more robust than the SPM type. However, since the magnetic flux returns inside the mover core, the output is lowered compared with the SPM type.

C.2 Surface-mounted Permanent Magnet (SPM)

The mover and the stator of SPM motor is displayed in Figure C.1(b). The Surface-mounted Permanent Magnet motor is a model in which the structure magnet is stuck on the surface of the mover. When a large impact is applied to the stator, the spiral motor may be damaged. Since this type of surface magnet can produce greater thrust than the magnet embedding type (IPM type), the SPM type is looking at the use as a direct acting joint of the robot. Three phase windings are wound on both sides of the stator.

(a) Stator and Mover of IPM Prototype

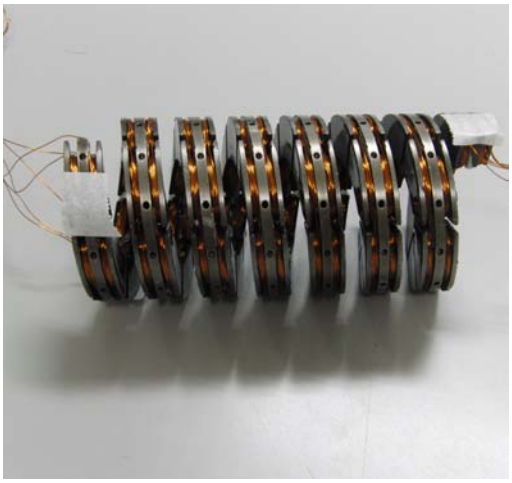

(b) Stator of IPM Prototype

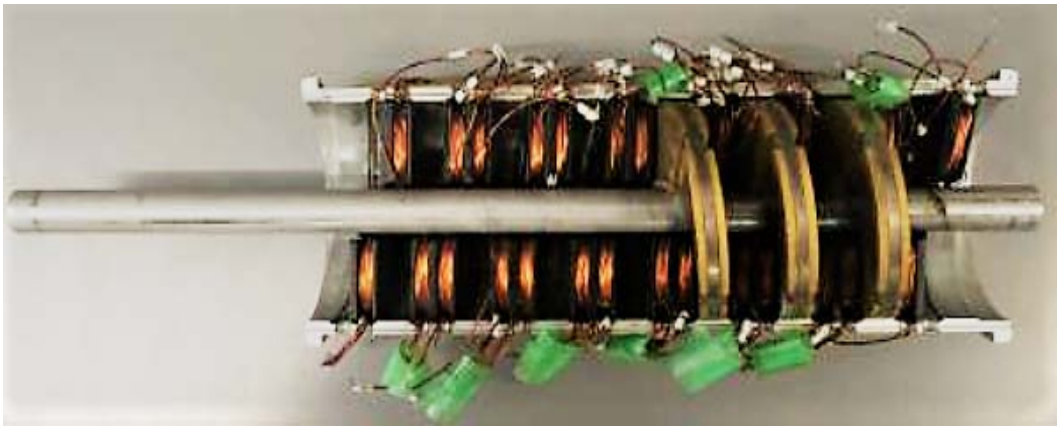

(c) Stator and Mover of SPM Prototype

Figure C.1: Stator and Mover of IPM and SPM Prototype

Acknowledgements

First of all, I am deeply thankful to my supervisor Professor Yasutaka Fujimoto, who gave me the opportunity to work in this interesting subject and grow up professionally. Secondly, I would like to thank my supervisor Professor Alessandro Beghi that encouraged me in this activity, Professor Roberto Oboe for the suggestions.
I would like to extend my gratitude to Masato Koyama who helped me with kindness throughout this work.
Also I would like to thank Yokohama National University for accepting me during my thesis and University of Padova for these years of study.
A lovely thanks goes to my beloved Giovanni, who helped me to overcome obstacle and has always been by my side.
A special thanks is for my family, my father Claudio, my mother Mirca and my sister Denyse, who helped me as only a family can do, with love and patience.
Finally, a big thanks to my Italian university colleagues, Sara, Gioela, Andrea, Massimiliano, my friends and Japanese laboratory's members who made this experience unforgettable.

References

[1] Hermann M., Pentek T., Otto B., "Design Principles for Industrie 4.0 Scenarios",IEEE 2016 49th Hawaii International Conference on System Sciences, pp 3928-3937, 2016.

[2] Y.Fujimoto, et al.,"Modelling and Control of a High-thrust Direct-Drive Spiral Motor", Proc. IEEJ International Power Electronics Conference, 24F1-4, pp.2222-2229, 2010.

[3] Y.Fujimoto, T. Kominami and H. Hamada, "Development and Analysis of a High Thrust Force Direct-Drive Linear Actuator", IEEE Transactions on Industrial Electronics, Vol. 56.

[4] M.Koyama and Y.Fujimoto,"Improvement of Position Tracking and Magnetic-Levitation Control Based on Optimal Control for Helical Motor",proc. IEEE Industrial Electronics Society Annual Conference (IECON), Florence, 2016.10 (to be presented)

[5] M.Koyama and Y.Fujimoto,"Zero Power Control Based on External Force Feedback for Helical Motor",IEEJ Transactions of Industry Applications, Vol. 5, No.4, pp.314-320, 2016.

[6] D.-W. Gu, P. Hr. Petkov and M. M. Konstantinov, "Robust Control Design with MATLAB® " Springer Editor, Germany 2005.

[7] B. Siciliano, L. Sciavicco, L. Villani and G. Oriolo, "Robotics Modelling, Planning and Control" Springer Science & Business Media, 2010.

[8] P. Corke , "Robotics Vision and Control " Springer, 2011.

[9] A.Z.Shukor, Y. Fujimoto, "Force Control of Musculoskeletal Manipulator Driven By Spiral Motors", Automatika - Journal for Control, Measurement, Electronics, Computing and Communications, 2012

[10] S.Sasaki and Y.Fujimoto,"Development of Two-Link Manipulator Using Helical Motors", Proc. IEEJ International Workshop on Sensing, Actuation and Motion Control (SAMCON),(2015).

[11] Hun-ok Lim, Kousuke Maenisi and Masahiko Sunagawa, "Development of Collision Force Suppression Mechanism",International Conference on Control, Automation and Systems, 2032-2037, Seoul, Oct. 2008

[12] Sami Haddadin, Alin Albu-$Schäffer$, Alessandro De Luca, and Gerd Hirzinger, "Collision Detection and Reaction: A Contribution to Safe Physical Human-Robot Interaction", IEEE/RSJ International Conference on Intelligent Robots and Systems, Acropolis Convention Center, 3357-3363 Nice, France, Sept. 2008

[13] Jessica Bergamo and Yasutaka Fujimoto, "Robust Control of Parameter Fluctuations For Helical Motors," proc. IEEJ International Workshop on Sensing, Actuation, Motion Control, and Optimization, Nagaoka, 2017

[14] S.Sasaki and Y.Fujimoto,"Impact force control by Using Helical Motor", Proc. IEEJ International Workshop on Sensing, Actuation, Motion Control and Optimization,(2016).

[15] H. Kobayashi, S. Katsura and K. Ohnishi, "An Analysis of Parameter Variations of Disturbace Observer for Motion Control", IEEE Trans. Industrial Electronics, Vol.54, No. 6, pp. 3413-3421, (2007)

[16] K. Onishi, "Robust Motion Control by Disturbance Observer", Journal of the Robotics Society of Japan Vol. 11 (1993) No. 4 P 486-493 (in Japanese)

[17] K. Yamada, I. Murakami, Y. Ando, T. Hagiwara, Y. Imai and M. Kobayash, "The Parametrization of All Disturbance Observers", ICIC Vol. 2 (2008) No. 4 P 421-426